Title: White matter microstructure across the adult lifespan: A mixed longitudinal and cross-sectional study using advanced diffusion models and brain-age prediction

Authors: Dani Beck[1,2,3], Ann-Marie de Lange[1,2,4], Ivan I. Maximov[1,2], Geneviève Richard[2], Ole A. Andreassen[2,5], Jan E. Nordvik[6], Lars T. Westlye[1,2,5]

[1] Department of Psychology, University of Oslo, Oslo, Norway

[2] NORMENT, Division of Mental Health and Addiction, Oslo University Hospital & Institute of Clinical Medicine, University of Oslo, Oslo, Norway

[3] Sunnaas Rehabilitation Hospital HT, Nesodden, Oslo, Norway

[4] Department of Psychiatry, University of Oxford, Warneford Hospital, Oxford, UK

[5] KG Jebsen Centre for Neurodevelopmental Disorders, University of Oslo, Oslo, Norway

[6] CatoSenteret Rehabilitation Center, Son, Norway

* Corresponding authors: Dani Beck (dani.beck@psykologi.uio.no) & Lars T. Westlye (l.t.westlye@psykologi.uio.no), Department of Psychology, University of Oslo, PO Box 1094 Blindern, 0317 OSLO, Norway, phone: +47 22845000, Fax: +47 22845001

Declarations of interest: none.

Conflict of interest: none.

Abstract

The macro- and microstructural architecture of human brain white matter undergoes substantial alterations throughout development and ageing. Most of our understanding of the spatial and temporal characteristics of these lifespan adaptations come from magnetic resonance imaging (MRI), including diffusion MRI (dMRI), which enables visualisation and quantification of brain white matter with unprecedented sensitivity and detail. However, with some notable exceptions, previous studies have relied on cross-sectional designs, limited age ranges, and diffusion tensor imaging (DTI) based on conventional single-shell dMRI. In this mixed cross-sectional and longitudinal study (mean interval: 15.2 months) including 702 multi-shell dMRI datasets, we combined complementary dMRI models to investigate age trajectories in healthy individuals aged 18 to 94 years (57.12% women). Using linear mixed effect models and machine learning based brain age prediction, we assessed the age-dependence of diffusion metrics, and compared the age prediction accuracy of six different diffusion models, including diffusion tensor (DTI) and kurtosis imaging (DKI), neurite orientation dispersion and density imaging (NODDI), restriction spectrum imaging (RSI), spherical mean technique multi-compartment (SMT-mc), and white matter tract integrity (WMTI). The results showed that the age slopes for conventional DTI metrics (fractional anisotropy [FA], mean diffusivity [MD], axial diffusivity [AD], radial diffusivity [RD]) were largely consistent with previous research, and that the highest performing advanced dMRI models showed comparable age prediction accuracy to conventional DTI. Linear mixed effects models and Wilk's theorem analysis showed that the 'FA fine' metric of the RSI model and 'orientation dispersion' (OD) metric of the NODDI model showed the highest sensitivity to age. The results indicate that advanced diffusion models (DKI, NODDI, RSI, SMT mc, WMTI) provide sensitive measures of age-related microstructural changes of white matter in the brain that complement and extend the contribution of conventional DTI.

Key words: ageing, white matter, multi-shell, longitudinal, diffusion, brain age

1. Introduction

The architecture of human brain white matter undergoes constant remodelling throughout life. Age-related trajectories of white matter macro- and microstructure typically reflect increases in anisotropy and decreases in diffusivity during childhood, adolescence and early adulthood (Krogsrud et al., 2016; Tamnes et al., 2018; Westlye et al., 2010), and subsequent anisotropy decreases and diffusivity increase in adulthood and senescence (Cox et al., 2016; Davis et al., 2009). While the field has primarily been dominated by cross-sectional studies, which by design lack information on individual trajectories (Schaie, 2005), longitudinal studies in the last decade have shown corresponding white matter changes in both development and ageing (Barrick et al., 2010; Bender et al., 2016; Bender & Raz, 2015; de Groot et al., 2016; Likitjaroen et al., 2012; Racine et al., 2019; Sexton et al., 2014; Storsve et al., 2016; Teipel et al., 2010). However, studies that have evaluated individual differences in change across a wide age range are rare (Bender et al., 2016).

White matter properties have commonly been investigated using traditional diffusion tensor imaging (DTI), and the DTI-based metrics fractional anisotropy (FA) as well as mean (MD), axial (AD), and radial (RD) diffusivity are highly sensitive to age (Cox et al., 2016; Sexton et al., 2014; Westlye et al., 2010; Yap et al., 2013). However, limitations of conventional DTI metrics such as their inability to capture restricted non-Gaussian diffusion and lack of specificity to different diffusion pools (Pines et al., 2020) have motivated continued development of more advanced diffusion MRI (dMRI) models. These models include *diffusion kurtosis imaging* (DKI) (Jensen et al., 2005), which was developed to address the restricted diffusion or non-Gaussianity in the diffusion signal; *neurite orientation dispersion and density imaging* (NODDI) (Zhang et al., 2012), which models three types of microstructural environments: intra-cellular, extra-cellular, and an isotropic water pool responsible for the space occupied by cerebrospinal fluid (CSF); *white matter tract integrity* (WMTI) (Chung et al., 2018; Fieremans et al., 2011), which derives microstructural characteristics from intra- and extra-axonal environments; *restriction spectrum imaging* (RSI) (White et al., 2013), which applies linear mixture modelling to resolve a spectrum of length scales while simultaneously acquiring geometric information; and *spherical mean technique multi-compartment* (SMT mc) (Kaden, Kruggel, et al., 2016), a method for microscopic diffusion anisotropy imaging that is unconfounded by effects of fibre crossings and orientation dispersion.

Usually based on multi-shell acquisitions with several diffusion weightings (Andersson & Sotiropoulos, 2015; Jbabdi et al., 2012), these models can be broadly split into “signal” and “tissue” models (D. C. Alexander et al., 2019). Signal representations, such as DTI and DKI, describe the diffusion signal behaviour in a voxel without assumptions about underlying tissue,

but as the estimated parameters lack specificity, their characterisation of tissue microstructure remains indirect (Jelescu & Budde, 2017). Tissue models (NODDI, RSI, SMT-mc, and WMTI) involve estimations of the geometry of underlying tissue (Novikov et al., 2019), which may provide higher biological specificity and more precise measures of white matter microstructure and architecture (Jelescu & Budde, 2017; Novikov et al., 2019; Pines et al., 2020). However, despite tissue models being designed to increase specificity, they also require assumptions about the underlying microstructure that may not be fully accurate.

Building on the opportunities from big data in neuroimaging (S. M. Smith & Nichols, 2018), age related brain changes have recently been investigated using machine learning techniques such as brain age prediction; the estimation of the 'biological' age of a brain based on neuroimaging data (J. H. Cole et al., 2018; de Lange et al., 2019; Kaufmann et al., 2019; Franke et al., 2010; Richard et al., 2018). Predicting the age of a brain, and subsequently looking at the disparity between predicted and chronological age, can identify important individualised markers of brain integrity that may reveal risk of neurological and/or neuropsychiatric disorders (Kaufmann et al., 2019). While brain age prediction has grown more popular in recent years, most studies have used grey matter features for brain age prediction, while only few have exclusively (Tønnesen et al., 2020), or partly (James H Cole, 2019; Maximov et al., 2020; Richard et al., 2018; S. M. Smith, Elliott, et al., 2019; S. M. Smith, Vidaurre, et al., 2019) utilised dMRI. However, the brain-age prediction accuracy of advanced diffusion models such as RSI and NODDI are not known.

Including cross-sectional and longitudinal data obtained from 573 healthy individuals (with 702 multi-shell dMRI datasets) aged 18-94 years, the primary aim of this study was to offer a comprehensive description of normative age-related white matter trajectories in adulthood by comparing relevant curve parameters such as key deflection points and rate of change as well as age prediction accuracy of different dMRI metrics, with a particular focus on relatively novel parameters based on advanced (DKI, NODDI, RSI, SMT mc, and WMTI) and conventional (DTI) diffusion models of white matter coherence and microstructure.

First, we estimated the trajectories of each of the diffusion metrics across the age range. Secondly, we utilised three separate methods to compare the age-sensitivity of the diffusion models: i) we used linear mixed effect (lme) models including age, sex, and timepoint, ii) for each model, we ran fits with and without age terms and compared the fit likelihood values using Wilk's theorem (Wilks, 1938), iii) we used machine learning to predict age based on the diffusion metrics, and compared the prediction accuracy of the models. Thirdly, we looked at the derivatives of each function of the lme models' age curve to identify the point of change in trajectory for each diffusion metric. Based on previous work characterising age differences and

longitudinal changes with a range of diffusion MRI metrics (Benitez et al., 2018; Falangola et al., 2008; Jelescu et al., 2015; Kodiweera et al., 2016; Reas et al., 2017; Westlye et al., 2010), we expected the included metrics to show curvilinear relationships with age, with varying trajectories and deflection points possibly reflecting differential involvement and rate of change of the putative biological underpinnings during the different phases of brain ageing.

2. Methods and material

2.1. Description of sample

The initial sample included 754 multi-shell datasets of healthy participants from two integrated studies; the Tematisk Område Psykoser (TOP) (Tønnesen et al., 2018) and StrokeMRI (Richard et al., 2018). Following the removal of 52 datasets after quality checking (QC, see section 2.4), the final sample comprised 702 scans from 573 individuals, including longitudinal data (two time-points with 15.2 months interval) for 129 of the participants. Demographic information is summarised in Table 1 and Figure 1.

Exclusion criteria included neurological and mental disorders, and previous head trauma. Ethical guidelines followed those in line with the Declaration of Helsinki. The study has been approved by the Regional Ethics Committee and all participants provided written informed consent.

Table 1. Demographics of descriptive statistics pertaining to the study sample. N refers to datasets.

	Age		
	Mean ± SD	Min	Max
Full (mixed) sample (n = 702)	50.86 ± 16.61	18.52	94.67
Male (301, 42.88%)	49.45 ± 17.48	18.52	92.05
Female (401, 57.12%)	51.92 ± 15.86	18.63	94.67
Cross-sectional sample (n = 444)	47.61 ± 16.59	18.52	94.67
Male (214, 48.20%)	46.75 ± 16.71	18.52	92.05
Female (230, 51.80%)	48.57 ± 16.51	18.63	94.67
Longitudinal sample (n = 258)	56.60 ± 15.03	20.30	85.82
Male (44, 35.11%)	55.72 ± 17.78	20.30	85.82
Female (85, 65.89%)	55.65 ± 13.70	23.37	80.62

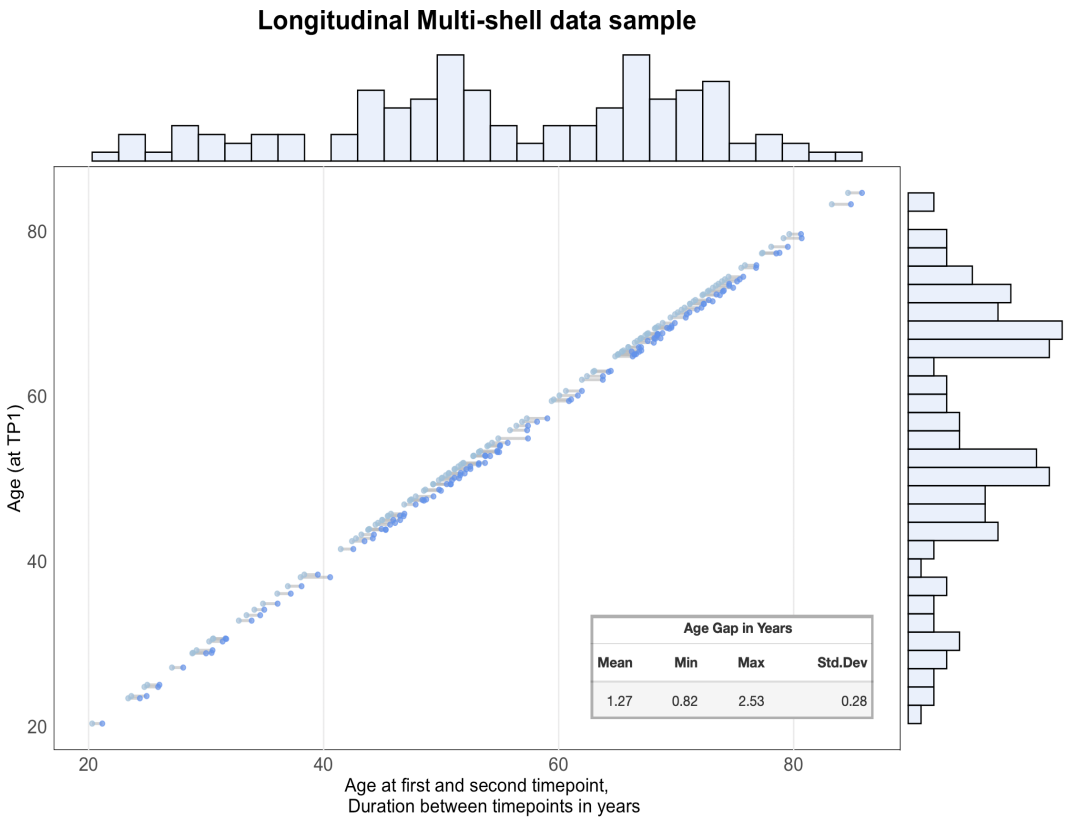

Figure 1. Interval between timepoint 1 and timepoint 2 for complete longitudinal sample, n = 258 (129 subjects). Histogram representing density of data points.

2.2. MRI acquisition

Imaging was performed at Oslo University Hospital on a General Electric Discovery MR750 3T scanner with a 32-channel head coil. dMRI data were acquired with a spin echo planar imaging (EPI) sequence with the following parameters: TR/TE/flip angle: 8,150 ms/83.1 ms/90°, FOV: 256 × 256 mm, slice thickness: 2 mm, in-plane resolution: 2 mm. We obtained 10 volumes of *b=0* and diffusion weighted data along 60 (b=1000 s/mm^2) and 30 (b=2000 s/mm^2) diffusion weighted volumes. In addition, 7 b=0 volumes with reversed phase-encoding direction were acquired for correction of susceptibility distortions.

2.3. Diffusion MRI processing

Processing steps followed a previously described pipeline (Maximov et al., 2019), including noise correction (Veraart et al., 2016), Gibbs ringing correction (Kellner et al., 2016), corrections for susceptibility induced distortions, head movements and eddy current induced distortions using topup (http://fsl.fmrib.ox.ac.uk/fsl/fslwiki/topup) and eddy (http://fsl.fmrib.ox.ac.uk/fsl/fslwiki/eddy) (Andersson & Sotiropoulos, 2016). Isotropic smoothing was carried out with a Gaussian kernel of 1 mm^3 implemented in the FSL function *fslmaths*. DTI was estimated using FSL tool *dtifit* and excluded the b=2000 shell from

the fit. Employing the multi-shell data, DKI and WMTI metrics were estimated using Matlab code (https://github.com/NYU-DiffusionMRI/DESIGNER), (Fieremans et al., 2011). NODDI metrics were derived using AMICO in Matlab (https://github.com/daducci/AMICO). SMT mc metrics were estimated with the original code (https://github.com/ekaden/smt). RSI metrics were estimated using in-house Matlab tools.

We selected 20 scalar metrics from the six models (DTI, DKI, NODDI, RSI, SMT mc, WMTI) based on recent studies (Benitez et al., 2018; De Santis et al., 2011; Hope et al., 2019; Jelescu et al., 2015; Kaden, Kelm, et al., 2016; Maximov et al., 2019; Pines et al., 2020). Models were also selected based on feasibility in relation to our acquisition protocol and availability of open source scripts. Figure 2 shows each of the included metrics for one participant, for illustrative purposes. All metrics and their corresponding abbreviations are summarised in Supplementary table 1). Brain age prediction was performed for each model, using all available metrics extracted from a range of regions-of-interest (see section 2.5).

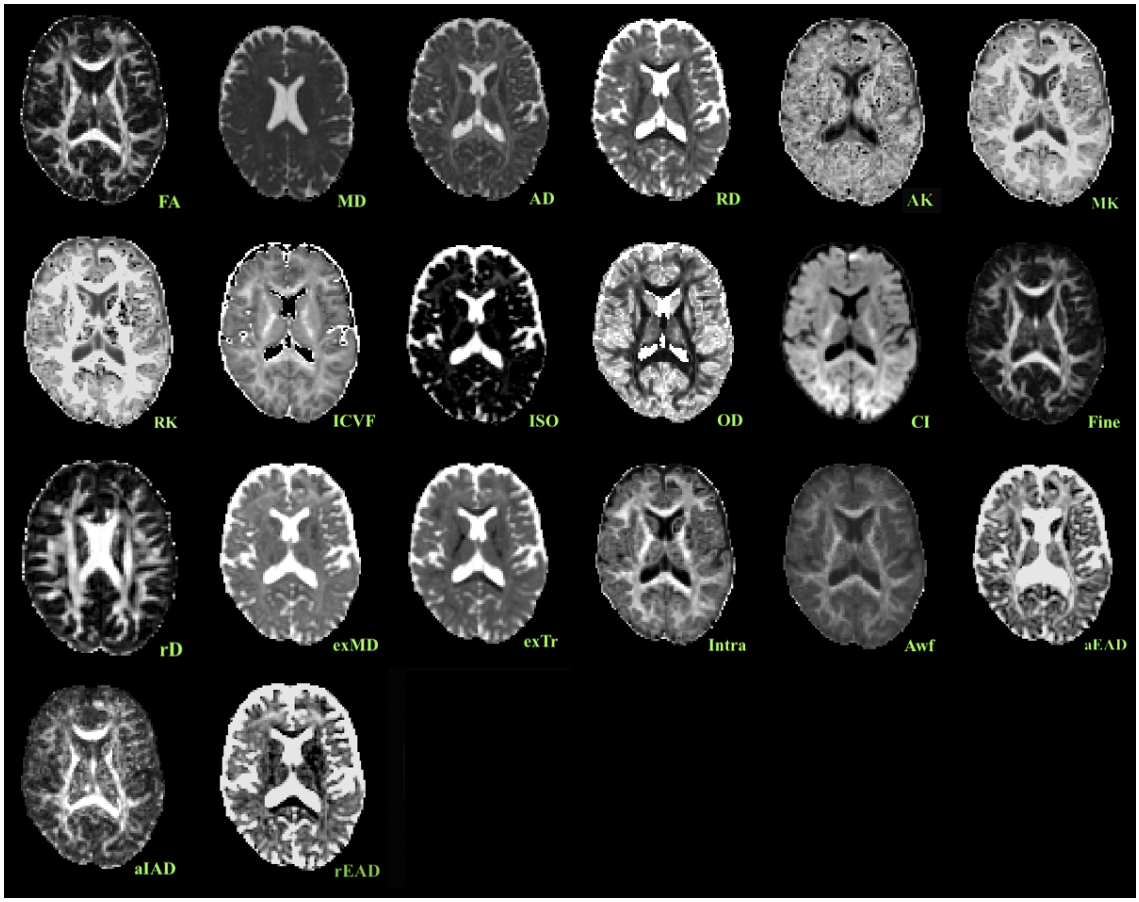

Figure 2. Diffusion metrics from one participant. **DTI**: *FA* (fractional anisotropy), *MD* (mean diffusivity), *AD* (axial diffusivity), *RD* (radial diffusivity). **DKI**: *AK* (axial kurtosis), *MK* (mean kurtosis), *RK* (radial kurtosis). **NODDI**: *ICVF* (intracellular volume fraction), *ISOVF* (isotropic volume fraction), *OD* (oriental dispersion). **RSI**: *CI* (cellular index), *Fine* (FA fine scale/slow compartment), *rD* (restricted diffusivity coefficient). **SMT mc**: *exMD* (extra cellular space), *exTr* (extra-cellular space transverse), *Intra* (intra axonal diffusivity). **WMTI**: *Awf* (axonal water fraction), *aEAD, aIAD* (axial extra and intra axonal diffusivity), *rEAD* (radial extra axonal diffusivity).

2.4. Quality checking procedure

We implemented a rigorous QC procedure to ensure data quality was not contaminated by motion, noise, or artefacts. Using a published approach (Roalf et al., 2016), we derived various quality assurance (QA) metrics (see Supplementary material; SI table 2), including temporal-signal-to-noise-ratio (TSNR). Outliers were manually checked and removed if deemed to have unsatisfactory data quality. A total of 52 datasets were removed, leaving the dataset at n = 702 scans. This dataset was put through the same visual inspection. As an additional step, images were manually inspected if TSNR Z scores deviated minus or plus 2.5 standard deviations from the mean. Following this step, the final dataset remained at 702 scans from 573 individuals.

2.5. Tract-Based-Spatial-Statistics

Voxelwise statistical analysis of the FA data was carried out using Tract-Based Spatial Statistics (TBSS) (S. M. Smith et al., 2006), as part of FSL (S. M. Smith et al., 2004). First, FA images were brain-extracted using BET (S. M. Smith, 2002) and aligned into a common space (FMRI58_FA template) using the nonlinear registration tool FNIRT (Andersson, Jenkinson, & Smith., 2007; Jenkinson et al., 2012), which uses a b-spline representation of the registration warp field (Rueckert et al., 1999). Next, the mean FA image of all subjects was created and thinned to create a mean FA skeleton that represents the centres of all tracts common to the group. Each subject's aligned FA data was then projected onto this skeleton. The mean FA skeleton was thresholded at FA > 0.2. This procedure was repeated for all metrics. *fslmeants* was used to extract the mean skeleton and 20 regions of interest (ROI) based on a probabilistic white matter atlas (JHU) (Hua et al., 2008) for each metric. Including the mean skeleton values, 420 features per individual were derived (20 metrics x 20+1 ROIs). Of these, 20 metrics were used for fitting of age curve trajectories, lme analysis, and Wilk's theorem analysis, while all 420 MRI features were used for age prediction. Number of MRI features can be found in Table 4. Additional voxelwise analysis were carried out on the 573 participants (excluding longitudinal measures) using the FSL tool Randomise with permutation-based statistics (Winkler et al., 2014) and threshold-free cluster enhancement method (TFCE; (S. Smith & Nichols, 2009)). 5000 permutations were run, where each diffusion metric was tested for its association with age. TBSS fill was used to create voxelwise statistical maps for each metric, which can be found in SI Figure 10.

2.6. Diffusion metric reproducibility

The validity and sensitivity of the different diffusion models essentially rely on the richness, quality and specific properties of the data used for model fitting. In order to assess the

reproducibility of the included advanced metrics (Maximov et al., 2015), we estimated the dMRI models using data obtained from different acquisition schemes varying the number of directions and maximum *b* value in 23 healthy participants with mean age 35.77 years (SD = 8.37, 56.5% women). This represented a sub-sample of the full sample. The following three acquisition schemes were compared: i) b=[1000,2000] with [60,30] directions, which is identical to the acquisition scheme used in the main analysis, ii) b=[1000,2000] with [60,60] directions and iii) b=[1000,2000,3000] with [60,60,60] directions. For each scheme we processed the data using an identical pipeline (Maximov et al., 2019) as described above and extracted the mean skeleton values for each metric. The comparisons between acquisition protocols were performed using box plots (SI Figure 4), scatterplots with age as a function of mean skeleton values (SI Figures 5), and Pearson's correlation coefficient plots, where protocol 1 is factored by protocol 3 (SI Figures 6).

2.7. Statistical analysis

All statistical analyses were carried out using the statistical environment R, version 3.6.0 (www.r-project.org/) (R Core Team, 2012) and Python 3.7.0 (www.python.org/).

2.8. Linear mixed effects models (lme)

To investigate the relationship between age and global mean skeleton values for each diffusion metric, lme analyses were performed using the *lme* function (Bates & Pinheiro, 1998) in R (R Core Team, 2012). In fitting the model, we scaled (z normalised) each variable and entered age, orthogonalised age^2, sex, and timepoint (TP) as fixed effects. Subject ID was entered as a random effect. For each diffusion metric M, we employed the following function:

$$M = A + B \times Age + C \times Age^2 + Sex + TP \qquad (1)$$

where A is the intercept, B is the age coefficient, and C is the coefficient of the orthogonalised quadratic age term (expressed as *poly(age,2)[,2]* in R). Age curves were obtained with predictions from the fitted model using the *predict* function in R and used for age curve trajectory figures. Visual inspection of residual plots did not reveal any obvious deviations from homoscedasticity or normality. The significance threshold was set at $p < 0.05$, and the results were corrected for multiple comparisons using the false discovery rate (FDR) adjustment (Benjamini & Hochberg, 1995).

To investigate the rate of change for each of the age curves at any point, we calculated their derivatives using numerical differentiation with finite differences (Burden & Faires,

2011). To compare the age-sensitivity of the models, we ran lme fits with and without age terms, and calculated the difference in likelihood ratios (Glover & Dixon, 2004). The significance of the age dependence was calculated using Wilk's theorem (Wilks, 1938) as $\sqrt{2(L_2 - L_1)}$, where L_2 is the likelihood ratio obtained from the models with age terms, and L_1 is the likelihood ratio obtained from the models without age terms.

2.9. Brain-age prediction

The XGBoost regressor model was used to run the brain age prediction (https://xgboost.readthedocs.io/en/latest/python/index.html), including a decision-tree-based ensemble algorithm that has been used in recent large-scale brain age studies (A.-M. G. de Lange et al., 2019; Kaufmann et al., 2019). Parameters were set to max depth = 3, number of estimators = 100, and learning rate = 0.1 (defaults). For each diffusion model (DTI, DKI, NODDI, RSI, SMT mc, WMTI), predicted age was estimated in a 10-fold cross validation, assigning a model-specific brain age estimate to each individual, as well as a multimodal brain age estimate based on all diffusion features. To investigate the prediction accuracy of each model, correlation analyses were run for predicted versus chronological age, and model-specific R^2, root mean square error (RMSE) and mean absolute error (MAE) were calculated. To statistically compare the prediction accuracy of the models, Z tests for correlated samples (Zimmerman, 2012) were run on the model-specific correlations between predicted and chronological age in a pairwise manner using

$$Z = (\beta_{m1} - \beta_{m2}) / \sqrt{\sigma_{m1}^2 + \sigma_{m2}^2 - 2\rho\sigma_{m1}\sigma_{m2}},$$

where “m1” and “m2” represent model 1 and model 2, the β terms represent the beta value from the regression fit, the σ terms represent their errors, and ρ represents the correlation between the two sets of associations. In order to assess the complementary value of the different models, we computed the correlations between the brain age predictions (Figure 6). The predictions were first corrected for age-bias using linear models (Le et al., 2018), and the residuals were used in the correlation analysis.

To evaluate the importance of each diffusion modality in the multimodal model, we ran an additional prediction model including only mean-skeleton values to reduce the number of highly correlated features in the regressor input, and calculated a) the proportion of the total *weight* contributed by each modality, where weight represents the number of times a feature is used to split the data across all trees, and b) *gain* values, which represent the improvement in

accuracy added by a feature to the branches it is on. To assess the significance of the general model performance, average RMSE was calculated for the multimodal model using cross validation with ten splits and ten repetitions and compared to a null distribution calculated from 1000 permutations.

3. Results

3.1. Diffusion metric reproducibility

The reproducibility of the estimated diffusion metrics based on data obtained with different acquisition schemes (described in 2.6) revealed overall high correlations between the mean skeleton values for all the model metrics. Highest overall reproducibility was observed for NODDI OD ($r(22) = 0.96$, $p < 0.001$) and RSI rD ($r(22) = 0.97$, $p < 0.001$). The lowest reproducibility was observed for WMTI radEAD ($r(22) = 0.44$, $p = 0.597$). Supplementary Table 4 and Supplementary Figures 4, 5, 6, and 7 show the results from the comparisons.

3.2. Age trajectories

Figure 3 shows the linear mixed effect model-derived age curves for each diffusion metric plotted as a function of age, where age curves are fitted with the predicted values of the lme models. Figure 4 shows all lme model-derived age curves from Figure 3 in standardised form in one plot. Figure 5 shows the derivatives of the lme fits, providing the estimated rate of change at every point (of age), including the point of change in trajectory for each model curve and the steepness of the turning point. Correlations between the metrics are available in the supplementary material (SI Figures 2 and 3) for both raw and standardised values respectively.

3.3. Comparing age curves

Figure 3 shows the estimated age curves for all metrics. Briefly, FA decreased steadily after the age of 30, with a steeper decline after the age of 50. MD, AD, and RD followed a reverse profile, with decreases in diffusivity until the 40's, whereby the trajectories subsequently increased thereafter. DKI metrics revealed curvilinear trajectories, with NODDI ICVF, RSI CI, SMT mc intra, and WMTI awf metrics following similar trajectories. RSI rD, NODDI ISOFV, RSI FA fine, and WMTI axIAD metrics followed decreasing trajectories from the offset. SMT mc extramd and extratrans, and WMTI radEAD followed similar trajectories to MD and RD. NODDI OD revealed a steady increase until older age where the slope stabilised thereafter. Lastly, WMTI axEAD showed u-trajectories.

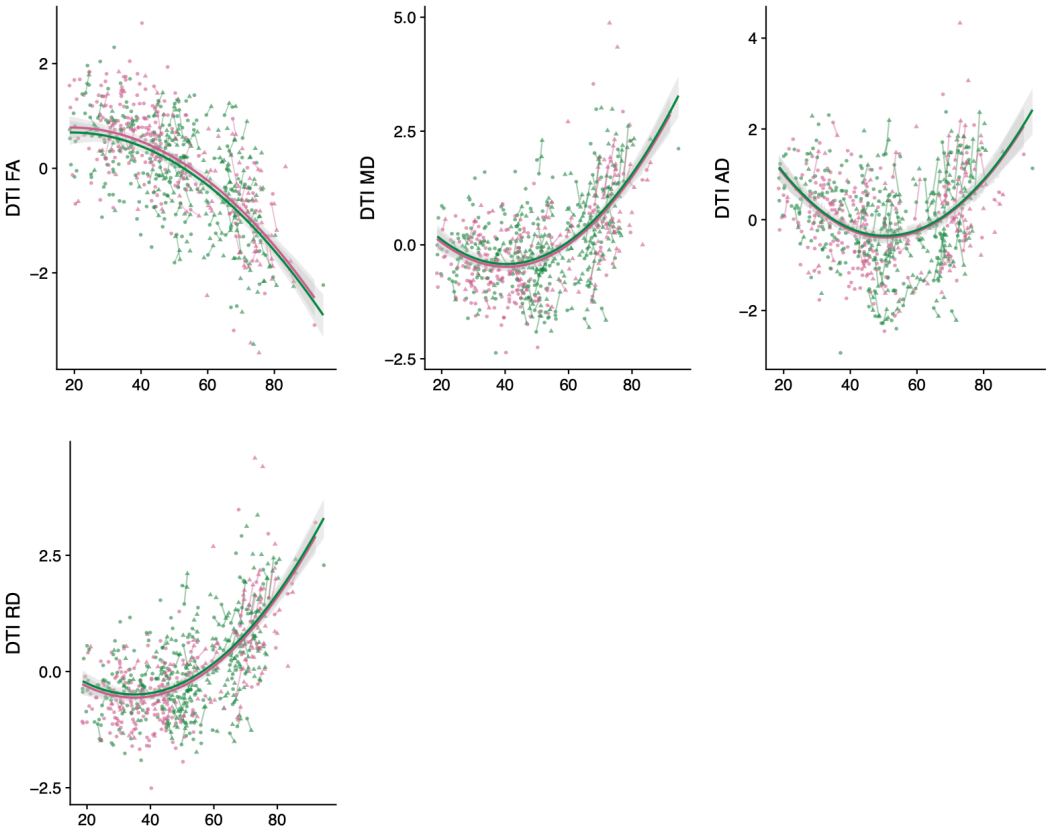

333

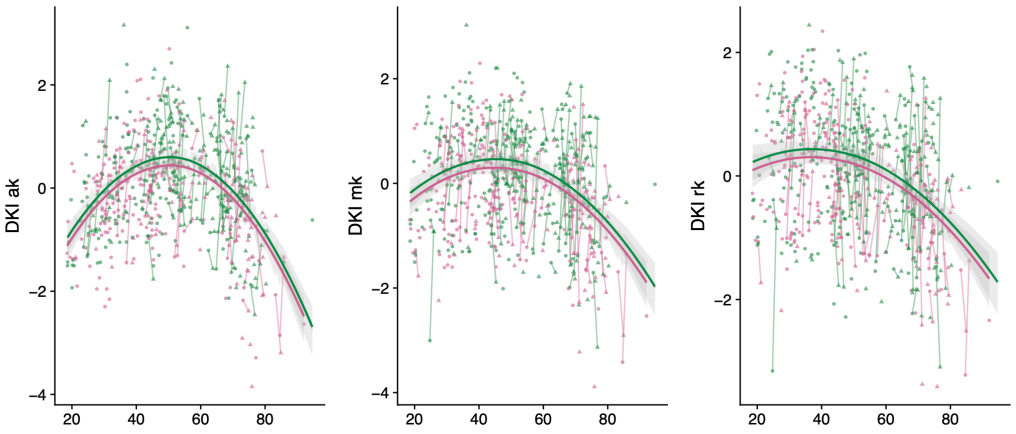

334

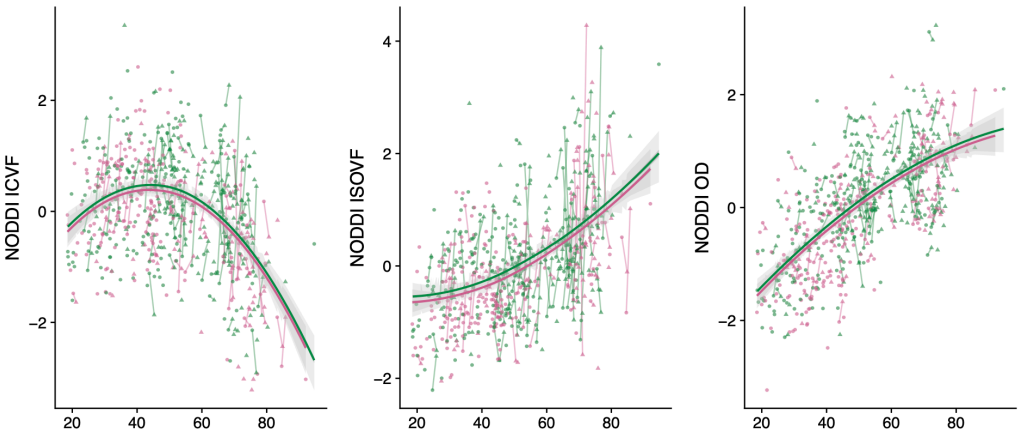

335

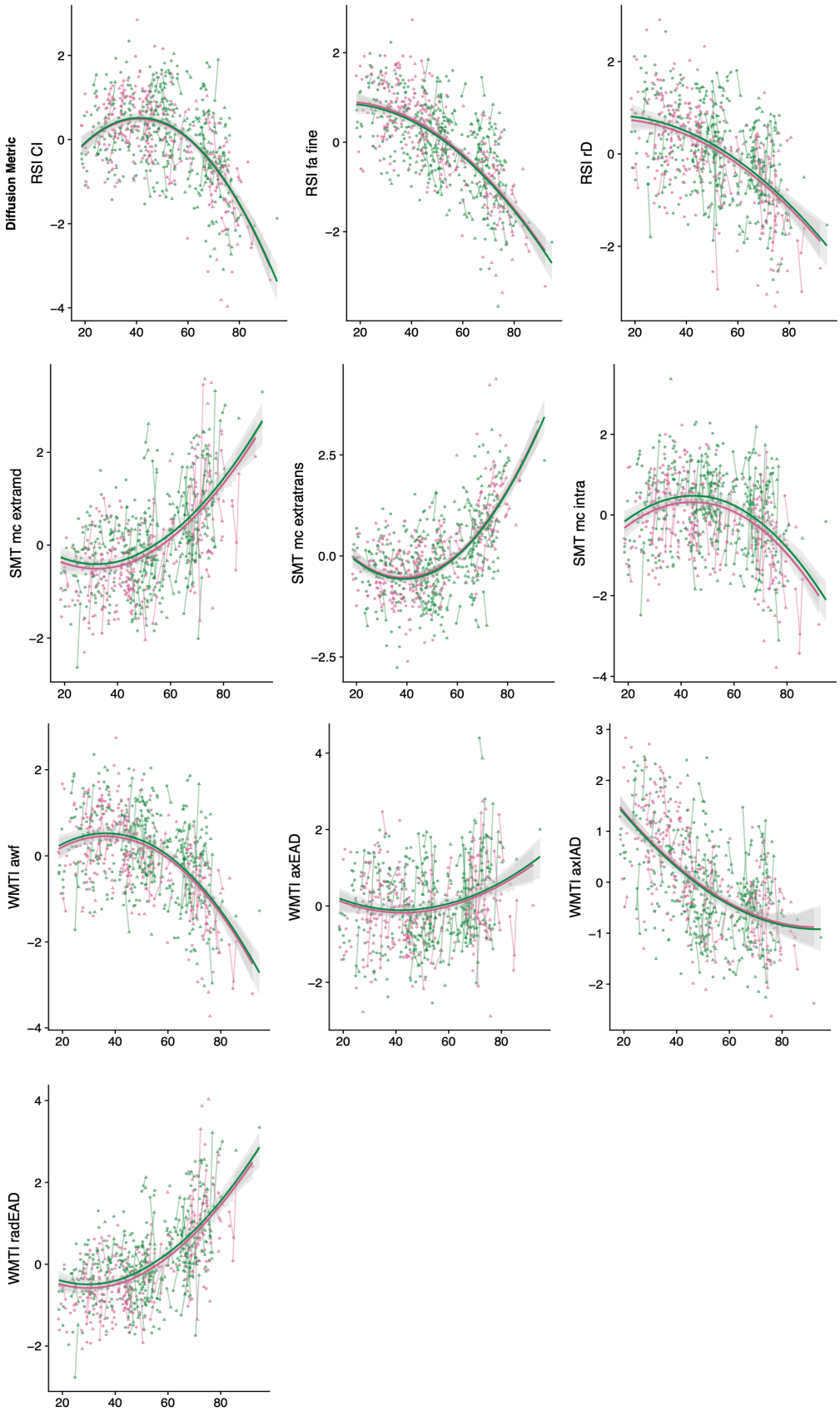

Figure 3. Age curves where each diffusion metric's standardised (z-score) mean skeleton value (y-axis) is plotted as a function of age (x-axis). Fitted lines made with lme-derived predicted values. Shaded areas represent 95% CI. Points connected by lines represent longitudinal data where circle is TP1 and triangle is TP2. Male subjects are represented by pink and female subjects by green.

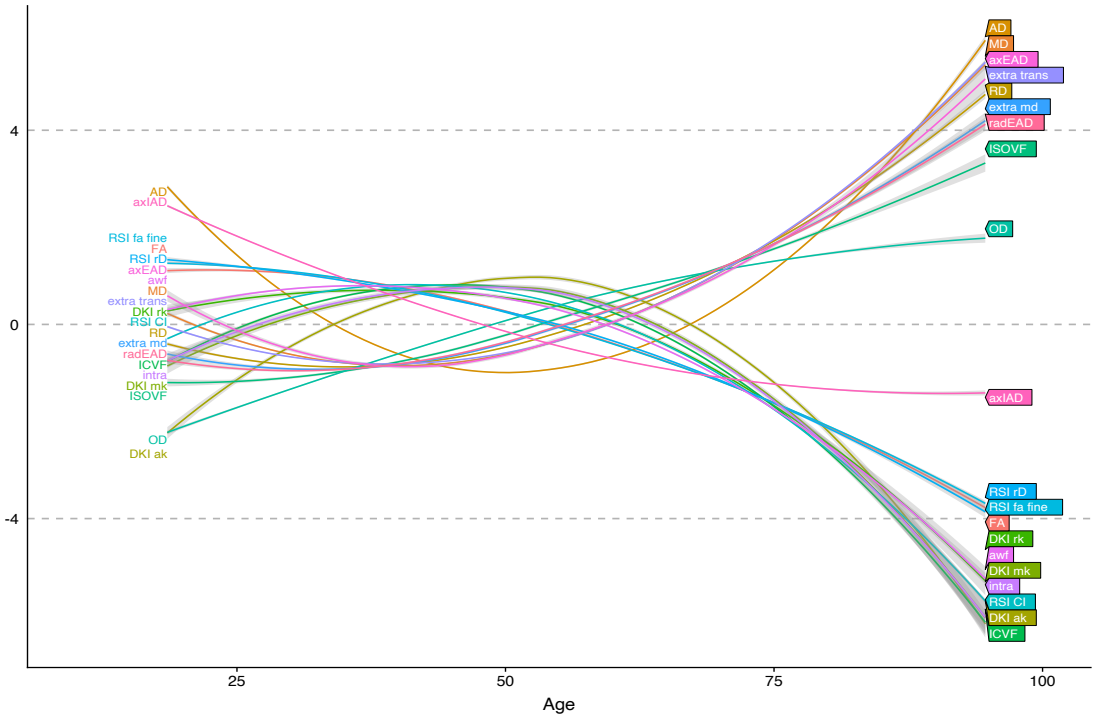

359 **Figure 4.** Plot displaying all lme-model derived age curves from Figure 3 in standardised form.

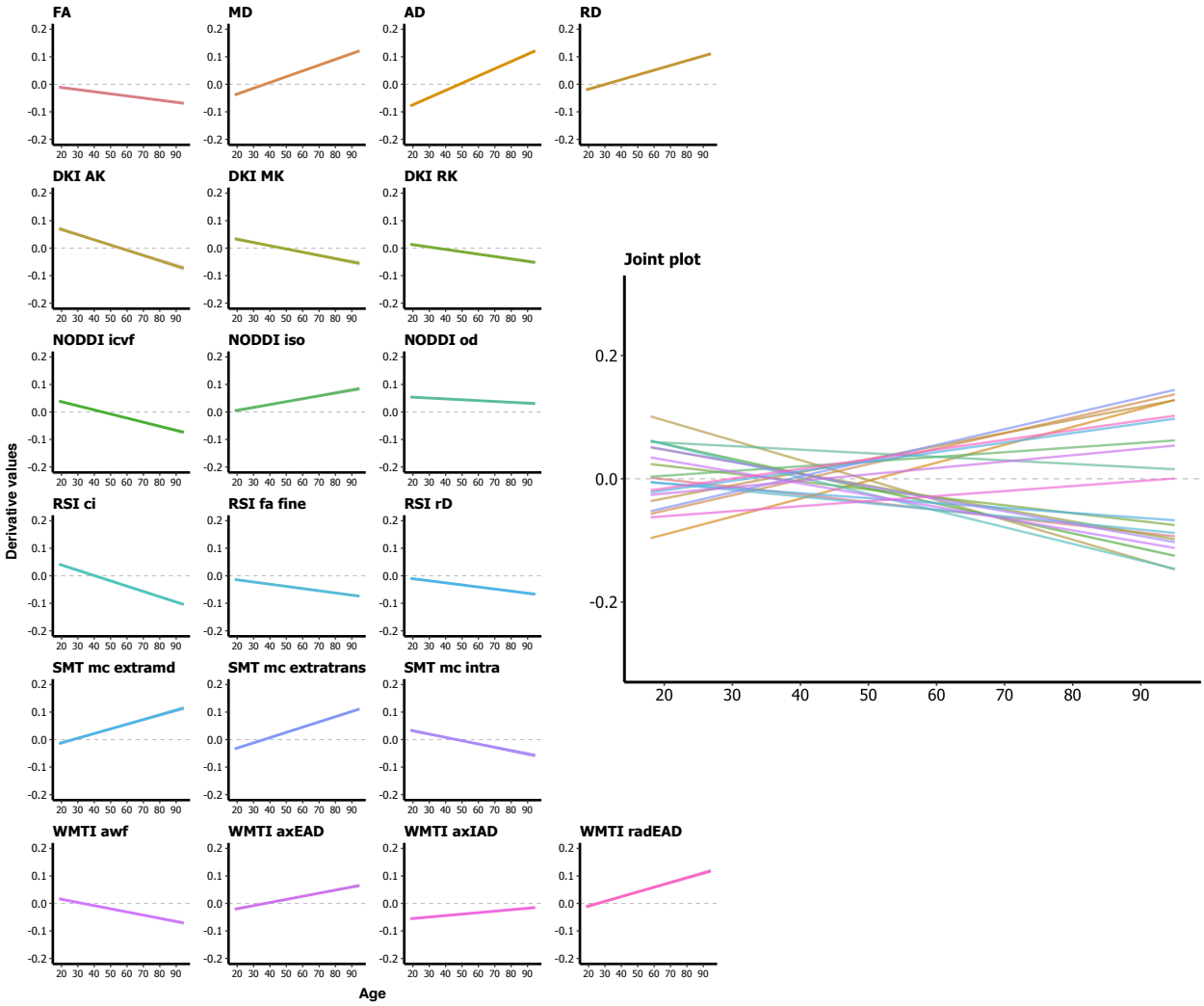

378 **Figure 5.** The derivative for each diffusion model, providing the estimated rate of change at every point. The
379 point on the x-axis where the fitted line crosses 0 on the y-axis represents the turning point of the age trajectory
380 for each metric.

Table 2. Linear mixed effect model results for each metric, where variables are *displayed with corresponding fixed effect estimates (β), (standard error), t-statistic, and FDR corrected P value.*

	FA	MD	AD	RD	DKI ak	DKI mk	DKI rk	NODDI icvf	NODDI isovf	NODDI OD	RSI CI	RSI fa fine	RSI rD	SMT mc extramd	SMT mc extratrans	SMT mc intra	WMTI awf	WMTI axEAD	WMTI axIAD	WMTI radEAD
Age	-0.66***	0.46***	0.03	0.59***	-0.12*	-0.24***	-0.32***	-0.33***	0.48***	0.67***	-0.48***	-0.69***	-0.54***	0.50***	0.56***	-0.26***	-0.49***	0.15***	-0.58***	0.57***
	(0.03)	(0.04)	(0.04)	(0.03)	(0.04)	(0.04)	(0.04)	(0.04)	(0.04)	(0.03)	(0.04)	(0.03)	(0.04)	(0.04)	(0.03)	(0.04)	(0.04)	(0.04)	(0.04)	(0.03)
	-20.76	13.19	0.71	18.02	-3.21	-5.95	-8.09	-8.52	13.31	21.62	13.79	-21.97	-14.89	14.31	16.66	-6.68	-13.33	3.51	-16.43	17.11
	4.96 x 10^{-41}	3.92 x 10^{-24}	1	2.95 x 10^{-35}	0.01	2.56 x 10^{-07}	9.15 x 10^{-12}	4.29 x 10^{-13}	2.02 x 10^{-24}	9.16 x 10^{-43}	1.44 x 10^{-25}	1.87 x 10^{-43}	3.60 x 10^{-28}	8.41 x 10^{-27}	3.01 x 10^{-32}	7.14 x 10^{-09}	1.87 x 10^{-24}	6.16 x 10^{-03}	1.02 x 10^{-31}	2.97 x 10^{-33}
Age^2	-0.17***	0.34***	0.40***	0.29***	-0.44***	-0.26***	-0.18***	-0.33***	0.10*	-0.08	-0.37***	-0.15***	-0.11*	0.21***	0.35***	-0.27***	-0.26***	0.14***	0.11*	0.21***
	(0.03)	(0.03)	(0.04)	(0.03)	(0.04)	(0.04)	(0.04)	(0.04)	(0.03)	(0.03)	(0.03)	(0.03)	(0.03)	(0.03)	(0.03)	(0.04)	(0.03)	(0.04)	(0.03)	(0.03)
	-5.57	10.30	10.63	9.37	-12.34	-7.15	-4.77	-9.04	3.11	-2.66	-11.04	-4.93	-3.16	6.46	10.99	-7.42	-7.51	3.63	3.36	6.91
	1.48 x 10^{-06}	2.22 x 10^{-17}	6.84 x 10^{-18}	4.00 x 10^{-15}	4.47 x 10^{-22}	1.26 x 10^{-09}	5.00 x 10^{-05}	5.00 x 10^{-14}	0.02	0.09	3.46 x 10^{-19}	2.60 x 10^{-05}	0.02	2.15 x 10^{-08}	4.59 x 10^{-19}	3.12 x 10^{-10}	9.88 x 10^{-11}	6.16 x 10^{-03}	0.01	2.17 x 10^{-09}
Sex	-0.09**	0.06	0.03	0.07*	0.14***	0.16***	0.13***	0.08	0.10*	0.07	0.02	-0.05	0.08	0.10*	-0.03	0.15***	0.07	0.06	-0.03	0.09*
	(0.03)	(0.03)	(0.04)	(0.03)	(0.04)	(0.04)	(0.04)	(0.04)	(0.03)	(0.03)	(0.03)	(0.03)	(0.03)	(0.03)	(0.03)	(0.04)	(0.03)	(0.04)	(0.03)	(0.03)
	-3.12	1.75	0.78	2.16	4.00	4.19	3.48	2.20	2.90	2.48	0.62	-1.55	2.24	2.90	-1.07	4.10	1.88	1.56	-1.00	2.86
	1.52 x 10^{-02}	0.55	1	0.22	1.06 x 10^{-03}	3.54 x 10^{-04}	4.53 x 10^{-03}	0.19	0.03	0.10	1	0.82	0.18	0.03	1	4.91 x 10^{-04}	0.41	0.81	1	0.03
Timepoint	0.01	0.02	0.03	0.01	0.07	0.04	0.02	0.04	0.05	0.02	0.03	0.001	-0.01	0.06	-0.02	0.04	0.03	0.03	-0.02	0.05
	(0.01)	(0.01)	(0.02)	(0.01)	(0.03)	(0.03)	(0.03)	(0.03)	(0.03)	(0.01)	(0.01)	(0.01)	(0.02)	(0.03)	(0.01)	(0.03)	(0.02)	(0.03)	(0.02)	(0.02)
	0.88	1.55	1.72	1.02	2.36	1.21	0.64	1.62	1.64	1.33	1.95	0.05	-0.30	2.31	-1.44	1.32	1.41	1.03	-0.66	2.19
	1	0.62	0.89	1	0.10	1	1	0.57	0.52	0.93	0.35	1	1	0.11	1	0.95	0.80	1	1	0.15
Observations	702	702	702	702	702	702	702	702	702	702	702	702	702	702	702	702	702	702	702	702
Log Likelihood	-651.72	-741.08	-853.38	-671.25	-885.78	-941.80	-945.41	-885.92	-882.34	-678.79	-748.66	-662.96	-829.12	-832.39	-703.69	-932.36	-849.65	-965.60	-816.35	-795.04
Akaike Inf. Crit.	1,317.44	1,496.15	1,720.76	1,356.50	1,785.56	1,897.60	1,904.81	1,785.84	1,778.69	1,371.58	1,511.33	1,339.91	1,672.24	1,678.79	1,421.39	1,878.73	1,713.30	1,945.20	1,646.69	1,604.09
Bayesian Inf. Crit.	1,349.27	1,527.98	1,752.59	1,388.33	1,817.39	1,929.43	1,936.64	1,817.67	1,810.52	1,403.40	1,543.15	1,371.74	1,704.06	1,710.62	1,453.21	1,910.55	1,745.13	1,977.02	1,678.52	1,635.92

Note: Age^2 represents the orthogonalised polynomial quadratic age term (Eq. 1)

*p<0.05; **p<0.01; ***p<0.001

3.4. Age sensitivity estimated using lme models

Results from the lme models revealed significant main effects of age on the global mean skeleton values for all diffusion metrics (see Table 2). An examination of the fixed effects estimates (β) and t-statistics for the age term allows for interpretation of the extent and direction of the linear association with age. Overall, the FA fine compartment of the RSI model was most sensitive to age ($\beta(125) = -0.69$, t = -21.97, $p < 0.001$). NODDI OD was the second most sensitive to age ($\beta(125) = 0.67$, t = 21.62, $p < 0.001$). The model least sensitive to age was DTI AD ($\beta(125) = 0.03$, t = 0.71, $p = 1$). For conventional DTI metrics, FA was the most age sensitive ($\beta(125) = -0.66$, t = -20.76, $p < 0.001$). No main effects of timepoint survived correction for multiple comparisons.

3.5. Age sensitivity estimated using Wilk's theorem

Table 3 shows the strength of the overall age variation for each metric estimated by the difference in likelihood values (described in Section 2.8). All metrics showed significant age dependence, with RSI FA fine as the most age sensitive (z = 18.79), followed by NODDI OD (z = 18.55) and DTI-based FA (z = 18.12). WMTI axEAD (z = 4.65) was the least age-dependant metric.

Table 3 Likelihood values from the lme models without age terms (L_1) and with age terms (L_2). The significance of the age dependence is estimated by the difference in likelihood values using Wilk's theorem. FDR corrected p-values = p^{corr}.

Model		L_1	L_2	Difference (z)	*p-value*	p^{corr}
DTI	FA	-815.86	-651.72	18.12	5.22×10^{-72}	1.04×10^{-70}
	MD	-848.36	-741.08	14.65	2.55×10^{-47}	5.10×10^{-46}
	AD	-900.66	-853.38	9.72	2.93×10^{-21}	5.86×10^{-20}
	RD	-820.44	-671.25	17.27	1.62×10^{-65}	3.24×10^{-64}
DKI	AK	-952.44	-885.78	11.55	1.12×10^{-29}	2.25×10^{-28}
	MK	-977.09	-941.80	8.40	4.71×10^{-16}	9.42×10^{-15}
	RK	-981.65	-945.41	8.51	1.83×10^{-16}	3.65×10^{-15}
NODDI	ICVF	-948.54	-885.92	11.19	6.40×10^{-28}	1.28×10^{-26}
	ISOVF	-957.61	-882.34	12.27	2.06×10^{-33}	4.13×10^{-32}
	OD	-850.84	-678.79	18.55	1.90×10^{-75}	3.80×10^{-74}
RSI	CI	-866.73	-748.66	15.37	5.28×10^{-52}	1.06×10^{-50}
	FA fine	-839.53	-662.96	18.79	2.07×10^{-77}	4.15×10^{-76}
	rD	-922.24	-829.12	13.65	3.62×10^{-41}	7.24×10^{-40}
SMT mc	Extra md	-929.01	-832.39	13.90	1.10×10^{-42}	2.20×10^{-41}
	Extra trans	-848.79	-703.69	17.03	9.71×10^{-64}	1.94×10^{-62}
	Intra	-973.21	-932.36	9.04	1.82×10^{-18}	3.64×10^{-17}
WMTI	AWF	-942.66	-846.37	13.88	1.52×10^{-43}	3.04×10^{-41}
	axEAD	-973.15	-962.32	4.65	1.98×10^{-05}	3.97×10^{-04}
	axIAD	-930.26	-816.35	15.09	3.38×10^{-50}	6.76×10^{-49}
	radEAD	-922.92	-795.04	15.99	2.91×10^{-56}	5.81×10^{-55}

3.6. Age sensitivity estimated using brain age

The model performances for the multimodal and model-specific brain age predictions are shown in Table 4. SI Figures 8 and 9 show the associations between predicted age and chronological age for each of the models. Figure 6 shows the pairwise correlations between predicted age for each model. Pairwise differences in the age prediction accuracy of the models are shown in Figures 7 and 8. SI Figure 1 shows the RMSE of the multimodal model prediction compared to a null distribution obtained from calculating 1000 permutations.

Table 4. Number of MRI variables (corresponding to the sum of metric features), root mean square error (RMSE), mean absolute error (MAE), correlation between predicted and chronological age (Pearson's r), and R^2 for each of the models. CI = confidence interval.

Model	MRI variables	RMSE	MAE	r [95% CI]	R^2 [95% CI]
DTI	84	9.35	7.30	0.83 [0.80, 0.85]	0.68 [0.64, 0.72]
DKI	63	12.19	9.82	0.68 [0.64, 0.72]	0.46 [0.41,0.52]
NODDI	63	9.15	7.31	0.83 [0.81, 0.86]	0.70 [0.65, 0.74]
RSI	63	9.84	7.68	0.81 [0.78, 0.83]	0.65 [0.61,0.69]
SMT mc	63	11.30	9.01	0.73 [0.70, 0.76]	0.54 [0.50, 0.58]
WMTI	84	9.37	7.40	0.83 [0.80, 0.85]	0.68 [0.64, 0.72]
Multimodal	420	8.80	6.99	0.85 [0.83, 0.87]	0.72 [0.69, 0.76]

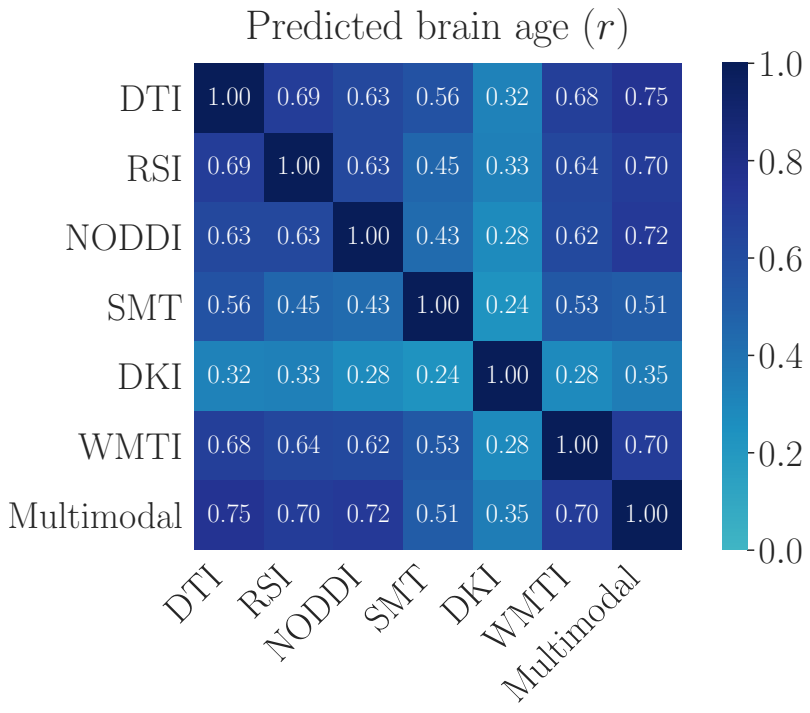

Figure 6. Correlation matrix for predicted brain age of each modality and the multimodal model. To account for age-bias (Le et al., 2018; S. M. Smith, Vidaurre, et al., 2019), the predicted age values were residualised for chronological age using linear models.

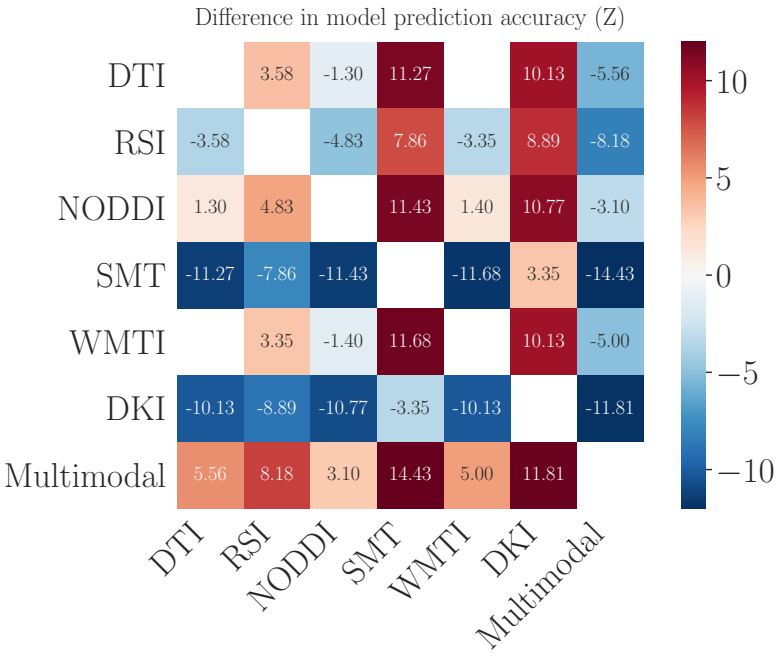

Figure 7. Matrix showing pairwise differences between the model prediction accuracies (correlations between predicted and chronological age), based on z tests for correlated samples.

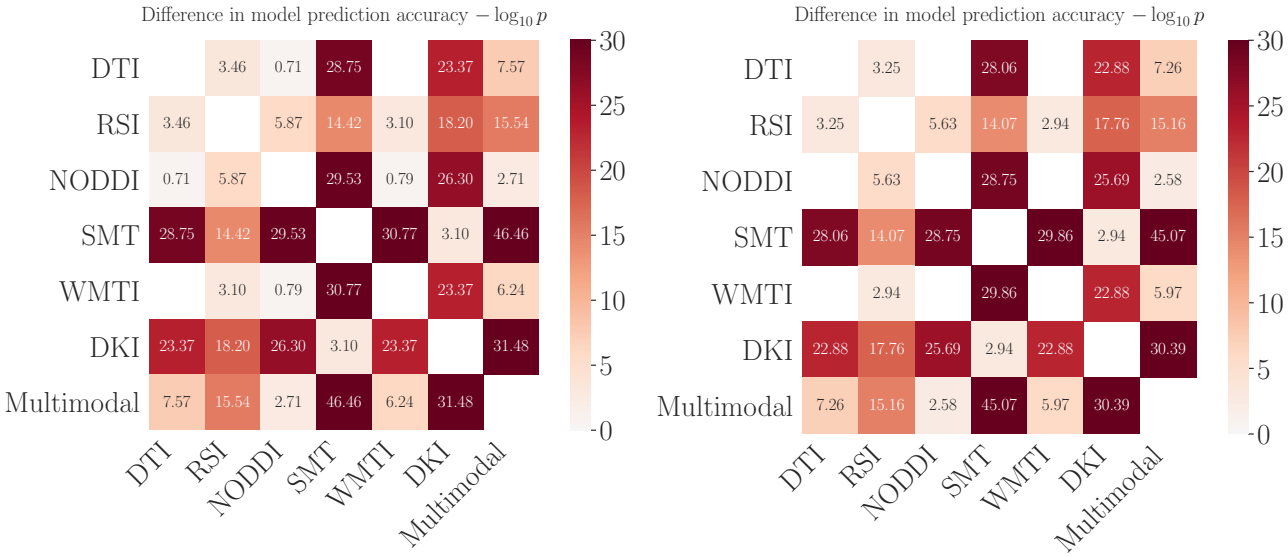

Figure 8. Log10(p) values of the pairwise differences between the model prediction accuracies. Higher numbers represent more significant differences. Left: uncorrected p-values. Right: P-values corrected for multiple comparisons using FDR, with non-significant (> 0.05) values masked out.

As visible from Table 4, the multimodal model showed the most accurate age prediction (r = 0.85, p < 0.001, 95% CI = [0.83, 0.87]), while the DKI model performed the worst (r = 0.68, p < 0.001, 95% CI = [0.64, 0.72]). As shown in Figures 7 and 8, the multimodal prediction accuracy was significantly higher than the accuracy of each of the other models, with the largest difference seen between the multimodal model and DKI. The differences in prediction

accuracy between DTI and RSI, and WMTI and NODDI did not survive correction for multiple comparisons. Figure 6 showed correlation coefficients of mean $r = 0.59$ (Std = 0.09) between the DTI, RSI, NODDI, SMT and WMTI predictions, while the DKI showed lower correlations with the other model predictions (mean $r = 0.29$, Std = 0.04).

To evaluate the relative importance of each modality, we ran an additional multimodal model including only mean-skeleton values to reduce the number of highly correlated features in the regressor input. Table 5 shows the total gain and the proportion of weight contributed by each modality to the total weight, indicating their relative contribution in the model training. The results revealed that the machine favoured the NODDI model in the training.

Table 5. Feature importance evaluated using a reduced multimodal model that included only mean skeleton values for each modality. Number of MRI variables (corresponding to the sum of metric features), percentage contribution to the total weight, and total gain for each modality.

Model	MRI variables	% of total weight	Total gain
DTI	4	20.09	163473.25
DKI	3	5.13	41747.63
NODDI	3	45.48	370129.31
RSI	3	4.85	39463.11
SMT mc	3	11.74	95534.98
WMTI	4	12.72	103545.15

4. Discussion

Ageing confers a range of structural brain alterations, affecting micro- and macrostructural properties of the neurocircuitry supporting cognitive and other complex brain functions. In the current mixed cross-sectional and longitudinal study, we compared age sensitivity and brain white matter age trajectories across the adult lifespan based on advanced and conventional dMRI models. The results from our comprehensive analysis approach, including age-curve trajectories, linear mixed effects models, Wilk's theorem analysis, and brain age prediction, showed high age sensitivity for all diffusion metrics, with comparable sensitivity between the highest performing advanced dMRI models and conventional DTI, and a moderate benefit of including all metrics in the same model. The mixed effects analyses and corresponding derivatives revealed variations in age trajectories between models, indicating that they may be sensitive to different underlying aspects of white matter ageing.

Our results showed that FA plateaued around the third decade with a steady decline in slope following the age of ~40, and an accelerated decrease in senescence (Figure 3). The other DTI metrics of MD, AD, and RD revealed decreases in diffusivity up until the 40-50-year age

mark, where the trajectories subsequently increase following a steady period. While these results to a large extent correspond with trajectories observed in previous studies (Cox et al., 2016; Davis et al., 2009; Westlye et al., 2010), a more defined inverted U-shape (Westlye et al., 2010) was less prominent in our study, likely due to a lack of younger participants below the age of 20. Interestingly, FA based on the relatively simple DTI model utilising only single-shell data offered one of the highest sensitivities to age, supporting that DTI provides sensitive measures of gross white matter anatomy and neuropathological changes (A. L. Alexander et al., 2008). The characteristic curvilinear trajectories of lifespan differences in conventional DTI metrics (Westlye et al., 2010) have previously been suggested to reflect a combination of protracted myelin-related maturation during childhood, adolescence and early adulthood (Lebel et al., 2008; Tamnes et al., 2010) and subsequent myelin loss during adulthood and senescence (Bartzokis et al., 2004). However, DTI metrics are unable to differentiate between intra- and extra-axonal compartments, and, in addition to the idiosyncratic changes in myeloarchitecture, they may be influenced by individual differences and changes in gross fiber architecture (e.g. crossing fibres) and axonal packing and density (Paus, 2010; Simmonds et al., 2014). The specific biological interpretation of DTI metrics essentially depends upon the local fiber architecture, and signal changes from DTI require careful interpretation, as the exact neurobiological underpinnings cannot be directly inferred. While speculative, utilising advanced dMRI models in addition to conventional DTI may provide more specificity in the interpretation of the results, and improve the descriptive precision of the tissue pathology by disentangling the various biological sources that are happening concurrently.

While several of the advanced dMRI models showed comparable results to DTI in terms of age sensitivity, they also showed visibly different age trajectories (Figure 3), including variation in turning points (Figure 4), indicating the age at which anisotropy and diffusivity measures change direction, and gradient of change (Figure 5), indicating rate of decline. The variation in turning points and gradient of change calculated using the derivates of each model informs us about the estimated rate of change at specific ages, in addition to the differential sensitivity between different metrics during different life phases. Although diffusion imaging cannot give direct access to neuronal processes on a cellular level, the varying estimated trajectories in advanced dMRI models potentially reflect differential involvement of the putative biological underpinnings during the different phases of brain ageing. Thus, metric-specific differences may reflect age-related pathological changes behind each dMRI model, helping us better pinpoint the age at which decline in white matter microstructure begins, which has important implications for interventive strategies aimed at promoting healthy ageing.

519 Although recent research has validated FA and RD metrics of DTI as being sensitive
520 markers to myelin (Lazari & Lipp, 2020), caution must be exerted in interpreting specific
521 underlying biology on the basis of DTI alone (Novikov et al., 2018). With this in mind,
522 combining tissue models such as NODDI, WMTI, RSI, and SMT mc may hold promise in
523 jointly reflecting measures more relatable to the neurobiological underpinnings of brain ageing.
524 The WMTI metrics for example have been validated for reflecting underlying biology both *in*
525 *vivo* (Jelescu et al., 2015, 2016) and *ex vivo* (Falangola et al., 2014; Kelm et al., 2016). WMTI
526 awf was found to relate to axonal density, whereas WMTI radEAD to some extent describes
527 the degree of myelination (Kelm et al., 2016) and relates to the extracellular environment filled
528 with interstitial fluid and circulating macromolecules, as well as blood vessels and perivascular
529 spaces (Nicholson & Hrabětová, 2017). The parameter maps from the NODDI model have
530 been claimed to exhibit a spatial pattern of tissue distribution consistent with the known brain
531 anatomy (Zhang et al., 2012), with existing maps showing the expected pattern of neurite
532 density (Jespersen et al., 2010), serving as an example of the feasibility provided by advanced
533 diffusion models to disentangle neurite density and orientation dispersion, two major factors
534 contributing to FA (Zhang et al., 2012). The RSI model diameter calculations have been shown
535 to correspond with the diameter of unmyelinated and myelinated axons in the rat brain (White
536 et al., 2013), suggesting a direct biological interpretation. Likewise, histological analyses have
537 shown that the SMT mc microscopic diffusion indices offer direct sensitivity to pathological
538 tissue alterations (Kaden et al. 2016). While not a tissue model, DKI provides a specific
539 measure of cellular compartments and membranes and is relatively unconfounded by
540 concentration of macromolecules, potentially providing a more specific indicator of tissue
541 properties than conventional DTI (Jensen et al., 2005).
542 In theory, the partly non-overlapping assumptions and biophysical properties of the
543 different diffusion MRI models offer a more comprehensive and complete view of the
544 manifold biological processes in brain development, ageing, and disorders when considered
545 jointly. In general, our findings of higher age prediction accuracy when combining different
546 models supports this view. However, not surprisingly, the relatively high correlations and
547 similar age-related trajectories of several of the different metrics also suggest a certain level of
548 redundancy. Further studies are needed to test the hypothesis that combining various diffusion
549 MRI models of brain macro- and microstructure increases the feasibility and precision of
550 multimodal data-driven brain phenotyping approaches (e.g. “fingerprinting”) towards more
551 specific clinical applications and prediction (Alnæs et al., 2018). With this in mind, including
552 the advanced models may not only improves specificity compared to conventional DTI, but
553 potentially provides additional information related to changes in myelination and axonal

554 rewiring, while specifically modelling microstructural features typically conflated by DTI, such
555 as neurite density, axonal diameter, and neurite orientation dispersion (D. C. Alexander et al.,
556 2019). Further research is needed to validate and develop dMRI models to better reflect the
557 different biological and geometrical properties of white matter. If assumptions of underlying
558 microstructure are valid, these advanced models represent a promising contribution to the
559 investigation of brain development and ageing, and aberrant brain biology in various clinical
560 conditions (D. C. Alexander et al., 2019).

561 While considering a range of diffusion models, it is important to note that each comes
562 with its respective limitations. NODDI has been particularly criticised in recent years, with
563 research suggesting the model assumptions are invalid (Lampinen et al., 2017). NODDI
564 provides estimates of geometric parameters only, with there being an absence of any direct
565 diffusivity estimation (Jelescu et al., 2015). DKI, like DTI, is limited in specificity as it can be
566 affected by different features of tissue microstructure. Thus, the biophysical model that relates
567 DKI parameters directly to white matter microstructure (WMTI, (Fieremans et al., 2011)) was
568 proposed. However, assumptions made in WMTI may be oversimplifying, which could lead to
569 bias in the estimated parameters in addition to reduced information about the microstructure.
570 WMTI parameter estimation accuracy is also said to progressively degrade with higher
571 orientation dispersion (Jelescu et al., 2015).

572 The SMT mc model overcomes limitations in WMTI (Fieremans et al., 2011) and
573 NODDI (Zhang et al., 2012) as it makes no assumptions about the neurite orientation
574 distribution (Kaden, Kelm, et al., 2016). However, it is limited by assuming that the effective
575 transverse diffusivity inside the neurites is zero, an approximation which may not hold for
576 unmyelinated axons and dendrites (Kaden, Kelm, et al., 2016), due to possible neurite
577 undulation on the microscopic scale (Nilsson et al., 2012). RSI, like most diffusion-based
578 techniques, suffers from low resolution and may best be utilised in supplement to high spatial
579 resolution sequences as part of a multimodal imaging protocol (Brunsing et al., 2017). For
580 example, the DTI model's limitation of being blind to crossing and bending fibres may be
581 resolved by the RSI model's multi-direction properties and ability to measure diffusion
582 orientation and length scale (White et al., 2013). Despite the limitations of each model, and
583 possible redundancy between them, assessing age-related white microstructural changes using
584 a combination of diffusion models can be advantageous in order to zero in on idiosyncratic
585 neuroanatomical and microstructural patterns (Alnæs et al., 2018). Biophysical models of
586 WMTI and SMT mc for example, adds the possibility for assessing the separate effect of
587 diffusion in intra- and extra-axonal space (Jelescu & Budde, 2017; Voldsbekk et al., 2020).

Some methodological limitations must also be addressed. One concern is that of averaging over regions of interests and the entire white matter skeleton, which is complicated by the direction and magnitude of age associations varying regionally. Recent findings (Tønnesen et al., 2020) found that the global mean skeleton model outperformed region of interest-based single-metric models, providing evidence for relevant information required for brain age prediction is captured at a global level. Indeed, previous studies have suggested that regional DTI-based indices of brain aging reflect relatively global processes (Penke et al., 2010; Westlye et al., 2010), which is also supported by a genetically informed approach demonstrating that a substantial proportion of the tract-wise heritability is accounted for by a general genetic factor (Gustavson et al., 2019). Secondly, we used FA to generate white matter skeletons. Future research should consider generating white matter skeletons based on advanced diffusion maps that are more resistant to crossing fibres.

Other strengths of the study must also be addressed. TBSS offers robust non-linear registration and skeletonization of individual FA maps, which allows both for subsequent voxel-wise analysis and extraction of ROI based summary stats using a range of white matter atlases. This approach is highly standardized, which promotes reproducibility and future meta-analyses. The direct test of the reproducibility of the included dMRI metrics across different acquisition schemes with a higher number of directions and *b*-values, supported the use of advanced computational dMRI models for data obtained using a clinically feasible acquisition protocol. The combination of advanced dMRI models based on multi-shell data is a key strength, which potentially provides more detailed features of the cellular environment from differential tissue responses elicited by the different *b*-values (Assaf & Basser, 2005; Clark et al., 2002; Pines et al., 2020).

The study also included a relatively large sample and benefitted from all participants having been scanned with the same MRI scanner. Additionally, with cross-sectional studies being limited by between-subject variance and possible cohort effects (Schaie, 2005), the current study profits from a mixed cross-sectional and longitudinal design, where participants can be used as their own baseline (Sexton et al., 2014). However, the longitudinal aspect of our study had some limitations, including the short interval duration, and the low sample size compared to the cross-sectional sample. Consequently, the main results were largely driven by cross sectional data despite the mixed cross-sectional and longitudinal nature of the design. Future research should aim to adopt fully longitudinal designs over several time points in order to evaluate individual differences in change over time, preferably over wide age ranges.

Although the advanced dMRI models offered new insight into age sensitivity (such as the relatively high performance of RSI and NODDI for age prediction) and differences in age

trajectories, the biological interpretation of these metrics require further validation. Continued development and validation of more optimal diffusion models that better reflect biological properties of the brain is needed, and future research should take into account the impact of a range of potential factors that may mediate brain and cognitive development (Alnæs et al., 2020) and ageing (Lindenberger, 2014), such as pre- and perinatal events, socio-demographical factors, education, lifestyle, cardiometabolic risk factors, and genetics.

In conclusion, characterising changes in white matter microstructure over the human lifespan is critical for establishing robust models of normative neurodevelopment and ageing, which in turn can help us to better understand deviations from healthy age trajectories. The current study demonstrates that while advanced and conventional dMRI models show comparable age-sensitivity, multi-shell diffusion acquisition and advanced dMRI models can contribute to measuring multiple, complementary aspects of white matter characteristics. Further developing dMRI models in terms of biological tissue specificity remains a challenging yet important goal for understanding white matter development across the human lifespan.

Acknowledgements and funding

The study is supported by the Research Council of Norway (223273, 249795, 248238, 286838), the South-Eastern Norway Regional Health Authority (2014097, 2015044, 2015073, 2016083, 2018037, 2018076), the Norwegian ExtraFoundation for Health and Rehabilitation (2015/FO5146), KG Jebsen Stiftelsen, ERA-Net Cofund through the ERA PerMed project 'IMPLEMENT', and the European Research Council under the European Union's Horizon 2020 research and Innovation program (ERC StG, Grant 802998).

5. References

Alexander, A. L., Lee, J. E., Lazar, M., & Field, A. S. (2008). *Diffusion Tensor Imaging of the Brain*. 26.

Alexander, D. C., Dyrby, T. B., Nilsson, M., & Zhang, H. (2019). Imaging brain microstructure with diffusion MRI: Practicality and applications. *NMR in Biomedicine*, *32*(4), e3841. https://doi.org/10.1002/nbm.3841

Alnæs, D., Kaufmann, T., Doan, N. T., Córdova-Palomera, A., Wang, Y., Bettella, F., Moberget, T., Andreassen, O. A., & Westlye, L. T. (2018). Association of Heritable

Cognitive Ability and Psychopathology With White Matter Properties in Children and Adolescents. *JAMA Psychiatry*, *75*(3), 287. https://doi.org/10.1001/jamapsychiatry.2017.4277

Alnæs, D., Kaufmann, T., Marquand, A. F., Smith, S. M., & Westlye, L. T. (2020). Patterns of sociocognitive stratification and perinatal risk in the child brain. *Proceedings of the National Academy of Sciences*, *117*(22), 12419–12427. https://doi.org/10.1073/pnas.2001517117

Andersson, J. L. R., & Sotiropoulos, S. N. (2015). Non-parametric representation and prediction of single- and multi-shell diffusion-weighted MRI data using Gaussian processes. *NeuroImage*, *122*, 166–176. https://doi.org/10.1016/j.neuroimage.2015.07.067

Andersson, J. L. R., & Sotiropoulos, S. N. (2016). An integrated approach to correction for off-resonance effects and subject movement in diffusion MR imaging. *NeuroImage*, *125*, 1063–1078. https://doi.org/10.1016/j.neuroimage.2015.10.019

Assaf, Y., & Basser, P. J. (2005). Composite hindered and restricted model of diffusion (CHARMED) MR imaging of the human brain. *NeuroImage*, *27*(1), 48–58. https://doi.org/10.1016/j.neuroimage.2005.03.042

Barrick, T. R., Charlton, R. A., Clark, C. A., & Markus, H. S. (2010). White matter structural decline in normal ageing: A prospective longitudinal study using tract-based spatial statistics. *NeuroImage*, *51*(2), 565–577. https://doi.org/10.1016/j.neuroimage.2010.02.033

Bartzokis, G., Sultzer, D., Lu, P. H., Nuechterlein, K. H., Mintz, J., & Cummings, J. L. (2004). Heterogeneous age-related breakdown of white matter structural integrity: Implications for cortical "disconnection" in aging and Alzheimer's disease. *Neurobiology of Aging*, *25*(7), 843–851. https://doi.org/10.1016/j.neurobiolaging.2003.09.005

Bates, D. M., & Pinheiro, J. C. (1998). LINEAR AND NONLINEAR MIXED-EFFECTS MODELS. *Conference on Applied Statistics in Agriculture*. https://doi.org/10.4148/2475-7772.1273

Bender, A. R., & Raz, N. (2015). Normal-appearing cerebral white matter in healthy adults: Mean change over 2 years and individual differences in change. *Neurobiology of Aging*, *36*(5), 1834–1848. https://doi.org/10.1016/j.neurobiolaging.2015.02.001

Bender, A. R., Völkle, M. C., & Raz, N. (2016). Differential aging of cerebral white matter in middle-aged and older adults: A seven-year follow-up. *NeuroImage*, *125*, 74–83. https://doi.org/10.1016/j.neuroimage.2015.10.030

Benitez, A., Jensen, J. H., Falangola, M. F., Nietert, P. J., & Helpern, J. A. (2018). Modeling white matter tract integrity in aging with diffusional kurtosis imaging. *Neurobiology of Aging*, *70*, 265–275. https://doi.org/10.1016/j.neurobiolaging.2018.07.006

Benjamini, Y., & Hochberg, Y. (1995). Controlling the False Discovery Rate: A Practical and Powerful Approach to Multiple Testing. *Journal of the Royal Statistical Society: Series B (Methodological)*, *57*(1), 289–300. https://doi.org/10.1111/j.2517-6161.1995.tb02031.x

Brunsing, R., Schenker-Ahmed, N. M., White, N. S., Parsons, J. K., Kane, C., Kuperman, J., Bartsch, H., Kader, A. K., Rakow-Penner, R., Seibert, T. M., Margolis, D., Raman, S. S., McDonald, C. R., Farid, N., Kesari, S., Hansel, D., Shabaik, A., Dale, A. M., & Karow, D. S. (2017). Restriction Spectrum Imaging: An evolving imaging biomarker in prostate magnetic resonance imaging. *Journal of Magnetic Resonance Imaging : JMRI*, *45*(2), 323–336. https://doi.org/10.1002/jmri.25419

Chung, S., Fieremans, E., Wang, X., Kucukboyaci, N. E., Morton, C. J., Babb, J., Amorapanth, P., Foo, F.-Y. A., Novikov, D. S., Flanagan, S. R., Rath, J. F., & Lui, Y. W. (2018). White Matter Tract Integrity: An Indicator of Axonal Pathology after Mild Traumatic

706 Brain Injury. *Journal of Neurotrauma*, *35*(8), 1015–1020.
707 https://doi.org/10.1089/neu.2017.5320
708 Clark, C. A., Hedehus, M., & Moseley, M. E. (2002). In vivo mapping of the fast and slow
709 diffusion tensors in human brain. *Magnetic Resonance in Medicine*, *47*(4), 623–628.
710 https://doi.org/10.1002/mrm.10118
711 Cole, J. H., Ritchie, S. J., Bastin, M. E., Hernández, M. C. V., Maniega, S. M., Royle, N.,
712 Corley, J., Pattie, A., Harris, S. E., Zhang, Q., Wray, N. R., Redmond, P., Marioni, R.
713 E., Starr, J. M., Cox, S. R., Wardlaw, J. M., Sharp, D. J., & Deary, I. J. (2018). Brain
714 age predicts mortality. *Molecular Psychiatry*, *23*(5), 1385–1392.
715 https://doi.org/10.1038/mp.2017.62
716 Cole, James H. (2019). *Multi-modality neuroimaging brain-age in UK Biobank: Relationship*
717 *to biomedical, lifestyle and cognitive factors* [Preprint]. Neuroscience.
718 https://doi.org/10.1101/812982
719 Cox, S. R., Ritchie, S. J., Tucker-Drob, E. M., Liewald, D. C., Hagenaars, S. P., Davies, G.,
720 Wardlaw, J. M., Gale, C. R., Bastin, M. E., & Deary, I. J. (2016). Ageing and brain
721 white matter structure in 3,513 UK Biobank participants. *Nature Communications*,
722 *7*(1), 13629. https://doi.org/10.1038/ncomms13629
723 Davis, S. W., Dennis, N. A., Buchler, N. G., White, L. E., Madden, D. J., & Cabeza, R. (2009).
724 Assessing the effects of age on long white matter tracts using diffusion tensor
725 tractography. *NeuroImage*, *46*(2), 530–541.
726 https://doi.org/10.1016/j.neuroimage.2009.01.068
727 de Groot, M., Cremers, L. G. M., Ikram, M. A., Hofman, A., Krestin, G. P., van der Lugt, A.,
728 Niessen, W. J., & Vernooij, M. W. (2016). White Matter Degeneration with Aging:
729 Longitudinal Diffusion MR Imaging Analysis. *Radiology*, *279*(2), 532–541.
730 https://doi.org/10.1148/radiol.2015150103

de Lange, A.-M., Barth, C., Kaufmann, T., Maximov, I. I., van der Meer, D., Agartz, I., & Westlye, L. T. (2019). *Cumulative estrogen exposure, APOE genotype, and women's brain aging—A population-based neuroimaging study* [Preprint]. Neuroscience. https://doi.org/10.1101/826123

de Lange, A.-M. G., Kaufmann, T., van der Meer, D., Maglanoc, L. A., Alnæs, D., Moberget, T., Douaud, G., Andreassen, O. A., & Westlye, L. T. (2019). Population-based neuroimaging reveals traces of childbirth in the maternal brain. *Proceedings of the National Academy of Sciences*, *116*(44), 22341–22346. https://doi.org/10.1073/pnas.1910666116

De Santis, S., Gabrielli, A., Palombo, M., Maraviglia, B., & Capuani, S. (2011). Non-Gaussian diffusion imaging: A brief practical review. *Magnetic Resonance Imaging*, *29*(10), 1410–1416. https://doi.org/10.1016/j.mri.2011.04.006

Falangola, M. F., Guilfoyle, D. N., Tabesh, A., Hui, E. S., Nie, X., Jensen, J. H., Gerum, S. V., Hu, C., LaFrancois, J., Collins, H. R., & Helpern, J. A. (2014). Histological correlation of diffusional kurtosis and white matter modeling metrics in cuprizone-induced corpus callosum demyelination: DK AND WMM IN THE CUPRIZONE-INDUCED MOUSE BRAIN DEMYELINATION. *NMR in Biomedicine*, *27*(8), 948–957. https://doi.org/10.1002/nbm.3140

Falangola, M. F., Jensen, J. H., Babb, J. S., Hu, C., Castellanos, F. X., Di Martino, A., Ferris, S. H., & Helpern, J. A. (2008). Age-related non-Gaussian diffusion patterns in the prefrontal brain. *Journal of Magnetic Resonance Imaging*, *28*(6), 1345–1350. https://doi.org/10.1002/jmri.21604

Fieremans, E., Jensen, J. H., & Helpern, J. A. (2011). White matter characterization with diffusional kurtosis imaging. *NeuroImage*, *58*(1), 177–188. https://doi.org/10.1016/j.neuroimage.2011.06.006

Franke, K., Ziegler, G., Klöppel, S., & Gaser, C. (2010). Estimating the age of healthy subjects from T1-weighted MRI scans using kernel methods: Exploring the influence of various parameters. *NeuroImage*, *50*(3), 883–892. https://doi.org/10.1016/j.neuroimage.2010.01.005

Glover, S., & Dixon, P. (2004). Likelihood ratios: A simple and flexible statistic for empirical psychologists. *Psychonomic Bulletin & Review*, *11*(5), 791–806. https://doi.org/10.3758/BF03196706

Gustavson, D. E., Hatton, S. N., Elman, J. A., Panizzon, M. S., Franz, C. E., Hagler, D. J., Fennema-Notestine, C., Eyler, L. T., McEvoy, L. K., Neale, M. C., Gillespie, N., Dale, A. M., Lyons, M. J., & Kremen, W. S. (2019). Predominantly global genetic influences on individual white matter tract microstructure. *NeuroImage*, *184*, 871–880. https://doi.org/10.1016/j.neuroimage.2018.10.016

Hope, T. R., Selnes, P., Rektorová, I., Anderkova, L., Nemcova-Elfmarkova, N., Balážová, Z., Dale, A., Bjørnerud, A., & Fladby, T. (2019). Diffusion tensor and restriction spectrum imaging reflect different aspects of neurodegeneration in Parkinson's disease. *PLOS ONE*, *14*(5), e0217922. https://doi.org/10.1371/journal.pone.0217922

Hua, K., Zhang, J., Wakana, S., Jiang, H., Li, X., Reich, D. S., Calabresi, P. A., Pekar, J. J., van Zijl, P. C. M., & Mori, S. (2008). Tract probability maps in stereotaxic spaces: Analyses of white matter anatomy and tract-specific quantification. *NeuroImage*, *39*(1), 336–347. https://doi.org/10.1016/j.neuroimage.2007.07.053

Jbabdi, S., Sotiropoulos, S. N., Savio, A. M., Graña, M., & Behrens, T. E. J. (2012). Model-based analysis of multishell diffusion MR data for tractography: How to get over fitting problems. *Magnetic Resonance in Medicine*, *68*(6), 1846–1855. https://doi.org/10.1002/mrm.24204

Jelescu, I. O., & Budde, M. D. (2017). Design and Validation of Diffusion MRI Models of White Matter. *Frontiers in Physics*, *5*, 61. https://doi.org/10.3389/fphy.2017.00061

Jelescu, I. O., Veraart, J., Adisetiyo, V., Milla, S. S., Novikov, D. S., & Fieremans, E. (2015). One diffusion acquisition and different white matter models: How does microstructure change in human early development based on WMTI and NODDI? *NeuroImage*, *107*, 242–256. https://doi.org/10.1016/j.neuroimage.2014.12.009

Jelescu, I. O., Veraart, J., Fieremans, E., & Novikov, D. S. (2016). Degeneracy in model parameter estimation for multi-compartmental diffusion in neuronal tissue: Degeneracy in Model Parameter Estimation of Diffusion in Neural Tissue. *NMR in Biomedicine*, *29*(1), 33–47. https://doi.org/10.1002/nbm.3450

Jenkinson, M., Beckmann, C. F., Behrens, T. E. J., Woolrich, M. W., & Smith, S. M. (2012). FSL. *NeuroImage*, *62*(2), 782–790. https://doi.org/10.1016/j.neuroimage.2011.09.015

Jensen, J. H., Helpern, J. A., Ramani, A., Lu, H., & Kaczynski, K. (2005). Diffusional kurtosis imaging: The quantification of non-gaussian water diffusion by means of magnetic resonance imaging. *Magnetic Resonance in Medicine*, *53*(6), 1432–1440. https://doi.org/10.1002/mrm.20508

Jespersen, S. N., Bjarkam, C. R., Nyengaard, J. R., Chakravarty, M. M., Hansen, B., Vosegaard, T., Østergaard, L., Yablonskiy, D., Nielsen, N. Chr., & Vestergaard-Poulsen, P. (2010). Neurite density from magnetic resonance diffusion measurements at ultrahigh field: Comparison with light microscopy and electron microscopy. *NeuroImage*, *49*(1), 205–216. https://doi.org/10.1016/j.neuroimage.2009.08.053

Kaden, E., Kelm, N. D., Carson, R. P., Does, M. D., & Alexander, D. C. (2016). Multi-compartment microscopic diffusion imaging. *NeuroImage*, *139*, 346–359. https://doi.org/10.1016/j.neuroimage.2016.06.002

Kaden, E., Kruggel, F., & Alexander, D. C. (2016). Quantitative mapping of the per-axon diffusion coefficients in brain white matter: Quantitative Mapping of the Per-Axon Diffusion Coefficients. *Magnetic Resonance in Medicine*, *75*(4), 1752–1763. https://doi.org/10.1002/mrm.25734

Kaufmann, T., van der Meer, D., Doan, N. T., Schwarz, E., Lund, M. J., Agartz, I., Alnæs, D., Barch, D. M., Baur-Streubel, R., Bertolino, A., Bettella, F., Beyer, M. K., Bøen, E., Borgwardt, S., Brandt, C. L., Buitelaar, J., Celius, E. G., Cervenka, S., Conzelmann, A., … Westlye, L. T. (2019). Common brain disorders are associated with heritable patterns of apparent aging of the brain. *Nature Neuroscience*, *22*(10), 1617–1623. https://doi.org/10.1038/s41593-019-0471-7

Kellner, E., Dhital, B., Kiselev, V. G., & Reisert, M. (2016). Gibbs-ringing artifact removal based on local subvoxel-shifts. *Magnetic Resonance in Medicine*, *76*(5), 1574–1581. https://doi.org/10.1002/mrm.26054

Kelm, N. D., West, K. L., Carson, R. P., Gochberg, D. F., Ess, K. C., & Does, M. D. (2016). Evaluation of diffusion kurtosis imaging in ex vivo hypomyelinated mouse brains. *NeuroImage*, *124*, 612–626. https://doi.org/10.1016/j.neuroimage.2015.09.028

Kodiweera, C., Alexander, A. L., Harezlak, J., McAllister, T. W., & Wu, Y.-C. (2016). Age effects and sex differences in human brain white matter of young to middle-aged adults: A DTI, NODDI, and q-space study. *NeuroImage*, *128*, 180–192. https://doi.org/10.1016/j.neuroimage.2015.12.033

Krogsrud, S. K., Fjell, A. M., Tamnes, C. K., Grydeland, H., Mork, L., Due-Tønnessen, P., Bjørnerud, A., Sampaio-Baptista, C., Andersson, J., Johansen-Berg, H., & Walhovd, K. B. (2016). Changes in white matter microstructure in the developing brain—A longitudinal diffusion tensor imaging study of children from 4 to 11 years of age. *NeuroImage*, *124*, 473–486. https://doi.org/10.1016/j.neuroimage.2015.09.017

Lampinen, B., Szczepankiewicz, F., Mårtensson, J., van Westen, D., Sundgren, P. C., & Nilsson, M. (2017). Neurite density imaging versus imaging of microscopic anisotropy in diffusion MRI: A model comparison using spherical tensor encoding. *NeuroImage*, *147*, 517–531. https://doi.org/10.1016/j.neuroimage.2016.11.053

833 Lazari, A., & Lipp, I. (2020). *Can MRI measure myelin? Systematic review, qualitative*
834 *assessment, and meta-analysis of studies validating microstructural imaging with*
835 *myelin histology* [Preprint]. Neuroscience. https://doi.org/10.1101/2020.09.08.286518
836 Le, T. T., Kuplicki, R. T., McKinney, B. A., Yeh, H.-W., Thompson, W. K., Paulus, M. P., &
837 Tulsa 1000 Investigators. (2018). A Nonlinear Simulation Framework Supports
838 Adjusting for Age When Analyzing BrainAGE. *Frontiers in Aging Neuroscience*, *10*,
839 317. https://doi.org/10.3389/fnagi.2018.00317
840 Lebel, C., Walker, L., Leemans, A., Phillips, L., & Beaulieu, C. (2008). Microstructural
841 maturation of the human brain from childhood to adulthood. *NeuroImage*, *40*(3), 1044–
842 1055. https://doi.org/10.1016/j.neuroimage.2007.12.053
843 Likitjaroen, Y., Meindl, T., Friese, U., Wagner, M., Buerger, K., Hampel, H., & Teipel, S. J.
844 (2012). Longitudinal changes of fractional anisotropy in Alzheimer's disease patients
845 treated with galantamine: A 12-month randomized, placebo-controlled, double-blinded
846 study. *European Archives of Psychiatry and Clinical Neuroscience*, *262*(4), 341–350.
847 https://doi.org/10.1007/s00406-011-0234-2
848 Lindenberger, U. (2014). Human cognitive aging: Corriger la fortune? *Science*, *346*(6209),
849 572–578. https://doi.org/10.1126/science.1254403
850 Maximov, I. I., Alnæs, D., & Westlye, L. T. (2019). Towards an optimised processing pipeline
851 for diffusion magnetic resonance imaging data: Effects of artefact corrections on
852 diffusion metrics and their age associations in UK Biobank. *Human Brain Mapping*,
853 *40*(14), 4146–4162. https://doi.org/10.1002/hbm.24691
854 Maximov, I. I., Thönneßen, H., Konrad, K., Amort, L., Neuner, I., & Shah, N. J. (2015).
855 Statistical Instability of TBSS Analysis Based on DTI Fitting Algorithm: TBSS
856 analysis. *Journal of Neuroimaging*, *25*(6), 883–891. https://doi.org/10.1111/jon.12215
857 Maximov, I. I., van der Meer, D., de Lange, A.-M., Kaufmann, T., Shadrin, A., Frei, O.,
858 Wolfers, T., & Westlye, L. T. (2020). *Fast qualit **Y** con **T** rol me **T** hod fo **R** der **I** ved*

*diff**U** sion **M** etrics (**YTTRIUM**) in big data analysis: UK Biobank 18608 example* [Preprint]. Neuroscience. https://doi.org/10.1101/2020.02.17.952697

Nicholson, C., & Hrabětová, S. (2017). Brain Extracellular Space: The Final Frontier of Neuroscience. *Biophysical Journal*, *113*(10), 2133–2142. https://doi.org/10.1016/j.bpj.2017.06.052

Nilsson, M., Lätt, J., Ståhlberg, F., Westen, D., & Hagslätt, H. (2012). The importance of axonal undulation in diffusion MR measurements: A Monte Carlo simulation study: THE IMPORTANCE OF AXONAL UNDULATION IN DIFFUSION MR MEASUREMENTS. *NMR in Biomedicine*, *25*(5), 795–805. https://doi.org/10.1002/nbm.1795

Novikov, D. S., Fieremans, E., Jespersen, S. N., & Kiselev, V. G. (2019). Quantifying brain microstructure with diffusion MRI: Theory and parameter estimation. *NMR in Biomedicine*, *32*(4), e3998. https://doi.org/10.1002/nbm.3998

Novikov, D. S., Kiselev, V. G., & Jespersen, S. N. (2018). On modeling. *Magnetic Resonance in Medicine*, *79*(6), 3172–3193. https://doi.org/10.1002/mrm.27101

Paus, T. (2010). Growth of white matter in the adolescent brain: Myelin or axon? *Brain and Cognition*, *72*(1), 26–35. https://doi.org/10.1016/j.bandc.2009.06.002

Penke, L., Maniega, S. M., Murray, C., Gow, A. J., Valdes Hernandez, M. C., Clayden, J. D., Starr, J. M., Wardlaw, J. M., Bastin, M. E., & Deary, I. J. (2010). A General Factor of Brain White Matter Integrity Predicts Information Processing Speed in Healthy Older People. *Journal of Neuroscience*, *30*(22), 7569–7574. https://doi.org/10.1523/JNEUROSCI.1553-10.2010

Pines, A. R., Cieslak, M., Larsen, B., Baum, G. L., Cook, P. A., Adebimpe, A., Dávila, D. G., Elliott, M. A., Jirsaraie, R., Murtha, K., Oathes, D. J., Piiwaa, K., Rosen, A. F. G., Rush, S., Shinohara, R. T., Bassett, D. S., Roalf, D. R., & Satterthwaite, T. D. (2020). Leveraging multi-shell diffusion for studies of brain development in youth and young

adulthood. *Developmental Cognitive Neuroscience*, *43*, 100788. https://doi.org/10.1016/j.dcn.2020.100788

Racine, A. M., Merluzzi, A. P., Adluru, N., Norton, D., Koscik, R. L., Clark, L. R., Berman, S. E., Nicholas, C. R., Asthana, S., Alexander, A. L., Blennow, K., Zetterberg, H., Kim, W. H., Singh, V., Carlsson, C. M., Bendlin, B. B., & Johnson, S. C. (2019). Association of longitudinal white matter degeneration and cerebrospinal fluid biomarkers of neurodegeneration, inflammation and Alzheimer's disease in late-middle-aged adults. *Brain Imaging and Behavior*, *13*(1), 41–52. https://doi.org/10.1007/s11682-017-9732-9

Reas, E. T., Hagler, D. J., White, N. S., Kuperman, J. M., Bartsch, H., Cross, K., Loi, R. Q., Balachandra, A. R., Meloy, M. J., Wierenga, C. E., Galasko, D., Brewer, J. B., Dale, A. M., & McEvoy, L. K. (2017). Sensitivity of restriction spectrum imaging to memory and neuropathology in Alzheimer's disease. *Alzheimer's Research & Therapy*, *9*(1), 55. https://doi.org/10.1186/s13195-017-0281-7

Richard, G., Kolskår, K., Sanders, A.-M., Kaufmann, T., Petersen, A., Doan, N. T., Monereo Sánchez, J., Alnæs, D., Ulrichsen, K. M., Dørum, E. S., Andreassen, O. A., Nordvik, J. E., & Westlye, L. T. (2018). Assessing distinct patterns of cognitive aging using tissue-specific brain age prediction based on diffusion tensor imaging and brain morphometry. *PeerJ*, *6*, e5908. https://doi.org/10.7717/peerj.5908

Roalf, D. R., Quarmley, M., Elliott, M. A., Satterthwaite, T. D., Vandekar, S. N., Ruparel, K., Gennatas, E. D., Calkins, M. E., Moore, T. M., Hopson, R., Prabhakaran, K., Jackson, C. T., Verma, R., Hakonarson, H., Gur, R. C., & Gur, R. E. (2016). The impact of quality assurance assessment on diffusion tensor imaging outcomes in a large-scale population-based cohort. *NeuroImage*, *125*, 903–919. https://doi.org/10.1016/j.neuroimage.2015.10.068

Rueckert, D., Sonoda, L. I., Hayes, C., Hill, D. L. G., Leach, M. O., & Hawkes, D. J. (1999). Nonrigid registration using free-form deformations: Application to breast MR images.

IEEE Transactions on Medical Imaging, *18*(8), 712–721. https://doi.org/10.1109/42.796284

Schaie, K. W. (2005). What Can We Learn From Longitudinal Studies of Adult Development? *Research in Human Development*, *2*(3), 133–158. https://doi.org/10.1207/s15427617rhd0203_4

Sexton, C. E., Walhovd, K. B., Storsve, A. B., Tamnes, C. K., Westlye, L. T., Johansen-Berg, H., & Fjell, A. M. (2014). Accelerated Changes in White Matter Microstructure during Aging: A Longitudinal Diffusion Tensor Imaging Study. *Journal of Neuroscience*, *34*(46), 15425–15436. https://doi.org/10.1523/JNEUROSCI.0203-14.2014

Simmonds, D. J., Hallquist, M. N., Asato, M., & Luna, B. (2014). Developmental stages and sex differences of white matter and behavioral development through adolescence: A longitudinal diffusion tensor imaging (DTI) study. *NeuroImage*, *92*, 356–368. https://doi.org/10.1016/j.neuroimage.2013.12.044

Smith, S. M. (2002). Fast robust automated brain extraction. *Human Brain Mapping*, *17*(3), 143–155. https://doi.org/10.1002/hbm.10062

Smith, S. M., Elliott, L. T., Alfaro-Almagro, F., McCarthy, P., Nichols, T. E., Douaud, G., & Miller, K. L. (2019). *Brain aging comprises multiple modes of structural and functional change with distinct genetic and biophysical associations* [Preprint]. Neuroscience. https://doi.org/10.1101/802686

Smith, S. M., Jenkinson, M., Johansen-Berg, H., Rueckert, D., Nichols, T. E., Mackay, C. E., Watkins, K. E., Ciccarelli, O., Cader, M. Z., Matthews, P. M., & Behrens, T. E. J. (2006). Tract-based spatial statistics: Voxelwise analysis of multi-subject diffusion data. *NeuroImage*, *31*(4), 1487–1505. https://doi.org/10.1016/j.neuroimage.2006.02.024

Smith, S. M., Jenkinson, M., Woolrich, M. W., Beckmann, C. F., Behrens, T. E. J., Johansen-Berg, H., Bannister, P. R., De Luca, M., Drobnjak, I., Flitney, D. E., Niazy, R. K.,

937 Saunders, J., Vickers, J., Zhang, Y., De Stefano, N., Brady, J. M., & Matthews, P. M.
938 (2004). Advances in functional and structural MR image analysis and implementation
939 as FSL. *NeuroImage*, *23*, S208–S219.
940 https://doi.org/10.1016/j.neuroimage.2004.07.051
941 Smith, S. M., & Nichols, T. E. (2018). Statistical Challenges in "Big Data" Human
942 Neuroimaging. *Neuron*, *97*(2), 263–268. https://doi.org/10.1016/j.neuron.2017.12.018
943 Smith, S. M., Vidaurre, D., Alfaro-Almagro, F., Nichols, T. E., & Miller, K. L. (2019).
944 Estimation of brain age delta from brain imaging. *NeuroImage*, *200*, 528–539.
945 https://doi.org/10.1016/j.neuroimage.2019.06.017
946 Smith, S., & Nichols, T. (2009). Threshold-free cluster enhancement: Addressing problems of
947 smoothing, threshold dependence and localisation in cluster inference. *NeuroImage*,
948 *44*(1), 83–98. https://doi.org/10.1016/j.neuroimage.2008.03.061
949 Storsve, A. B., Fjell, A. M., Yendiki, A., & Walhovd, K. B. (2016). Longitudinal Changes in
950 White Matter Tract Integrity across the Adult Lifespan and Its Relation to Cortical
951 Thinning. *PLOS ONE*, *11*(6), e0156770. https://doi.org/10.1371/journal.pone.0156770
952 Tamnes, C. K., Østby, Y., Fjell, A. M., Westlye, L. T., Due-Tønnessen, P., & Walhovd, K. B.
953 (2010). Brain Maturation in Adolescence and Young Adulthood: Regional Age-Related
954 Changes in Cortical Thickness and White Matter Volume and Microstructure. *Cerebral*
955 *Cortex*, *20*(3), 534–548. https://doi.org/10.1093/cercor/bhp118
956 Tamnes, C. K., Roalf, D. R., Goddings, A.-L., & Lebel, C. (2018). Diffusion MRI of white
957 matter microstructure development in childhood and adolescence: Methods, challenges
958 and progress. *Developmental Cognitive Neuroscience*, *33*, 161–175.
959 https://doi.org/10.1016/j.dcn.2017.12.002
960 Teipel, S. J., Meindl, T., Wagner, M., Stieltjes, B., Reuter, S., Hauenstein, K.-H., Filippi, M.,
961 Ernemann, U., Reiser, M. F., & Hampel, H. (2010). Longitudinal Changes in Fiber
962 Tract Integrity in Healthy Aging and Mild Cognitive Impairment: A DTI Follow-Up

963 Study. *Journal of Alzheimer's Disease*, *22*(2), 507–522. https://doi.org/10.3233/JAD-
964 2010-100234
965 Tønnesen, S., Kaufmann, T., de Lange, A.-M. G., Richard, G., Doan, N. T., Alnæs, D., van der
966 Meer, D., Rokicki, J., Moberget, T., Maximov, I. I., Agartz, I., Aminoff, S. R., Beck,
967 D., Barch, D. M., Beresniewicz, J., Cervenka, S., Fatouros-Bergman, H., Craven, A. R.,
968 Flyckt, L., … Sellgren, C. (2020). Brain Age Prediction Reveals Aberrant Brain White
969 Matter in Schizophrenia and Bipolar Disorder: A Multisample Diffusion Tensor
970 Imaging Study. *Biological Psychiatry: Cognitive Neuroscience and Neuroimaging*,
971 S2451902220301683. https://doi.org/10.1016/j.bpsc.2020.06.014
972 Tønnesen, S., Kaufmann, T., Doan, N. T., Alnæs, D., Córdova-Palomera, A., Meer, D. van der,
973 Rokicki, J., Moberget, T., Gurholt, T. P., Haukvik, U. K., Ueland, T., Lagerberg, T. V.,
974 Agartz, I., Andreassen, O. A., & Westlye, L. T. (2018). White matter aberrations and
975 age-related trajectories in patients with schizophrenia and bipolar disorder revealed by
976 diffusion tensor imaging. *Scientific Reports*, *8*(1), 14129.
977 https://doi.org/10.1038/s41598-018-32355-9
978 Veraart, J., Fieremans, E., & Novikov, D. S. (2016). Diffusion MRI noise mapping using
979 random matrix theory. *Magnetic Resonance in Medicine*, *76*(5), 1582–1593.
980 https://doi.org/10.1002/mrm.26059
981 Voldsbekk, I., Maximov, I. I., Zak, N., Roelfs, D., Geier, O., Due-Tønnessen, P., Elvsåshagen,
982 T., Strømstad, M., Bjørnerud, A., & Groote, I. (2020). Evidence for wakefulness-
983 related changes to extracellular space in human brain white matter from diffusion-
984 weighted MRI. *NeuroImage*, *212*, 116682.
985 https://doi.org/10.1016/j.neuroimage.2020.116682
986 Westlye, L. T., Walhovd, K. B., Dale, A. M., Bjornerud, A., Due-Tonnessen, P., Engvig, A.,
987 Grydeland, H., Tamnes, C. K., Ostby, Y., & Fjell, A. M. (2010). Life-Span Changes of

988 the Human Brain White Matter: Diffusion Tensor Imaging (DTI) and Volumetry.
989 *Cerebral Cortex*, *20*(9), 2055–2068. https://doi.org/10.1093/cercor/bhp280
990 White, N. S., Leergaard, T. B., D'Arceuil, H., Bjaalie, J. G., & Dale, A. M. (2013a). Probing
991 tissue microstructure with restriction spectrum imaging: Histological and theoretical
992 validation. *Human Brain Mapping*, *34*(2), 327–346. https://doi.org/10.1002/hbm.21454
993 White, N. S., Leergaard, T. B., D'Arceuil, H., Bjaalie, J. G., & Dale, A. M. (2013b). Probing
994 tissue microstructure with restriction spectrum imaging: Histological and theoretical
995 validation. *Human Brain Mapping*, *34*(2), 327–346. https://doi.org/10.1002/hbm.21454
996 Wilks, S. S. (1938). The Large-Sample Distribution of the Likelihood Ratio for Testing
997 Composite Hypotheses. *The Annals of Mathematical Statistics*, *9*(1), 60–62.
998 https://doi.org/10.1214/aoms/1177732360
999 Winkler, A. M., Ridgway, G. R., Webster, M. A., Smith, S. M., & Nichols, T. E. (2014).
1000 Permutation inference for the general linear model. *NeuroImage*, *92*, 381–397.
1001 https://doi.org/10.1016/j.neuroimage.2014.01.060
1002 Yap, Q. J., Teh, I., Fusar-Poli, P., Sum, M. Y., Kuswanto, C., & Sim, K. (2013). Tracking
1003 cerebral white matter changes across the lifespan: Insights from diffusion tensor
1004 imaging studies. *Journal of Neural Transmission*, *120*(9), 1369–1395.
1005 https://doi.org/10.1007/s00702-013-0971-7
1006 Zhang, H., Schneider, T., Wheeler-Kingshott, C. A., & Alexander, D. C. (2012). NODDI:
1007 Practical in vivo neurite orientation dispersion and density imaging of the human brain.
1008 *NeuroImage*, *61*(4), 1000–1016. https://doi.org/10.1016/j.neuroimage.2012.03.072
1009 Zimmerman, D. W. (n.d.). *Correcting Two-Sample z and t Tests for Correlation: An*
1010 *Alternative to One-Sample Tests on Difference Scores*. 28.
1011